Behavior of Cs^+-UF_6^- ion-pair plasmas in radiofrequency quadrupole-dipole fields. II. Theory[a)]

Albert F. Wagner
Chemistry Division, Argonne National Laboratory, Argonne, Illinois 60439

(Received 5 August 1982; accepted for publication 28 October 1982)

The behavior of a flowing Cs^+-UF_6^- ion-pair plasma in the radiofrequency (rf) quadrupole-dipole fields of a mass filter has been studied theoretically. The theoretical calculations were designed to simulate the experimental observations of the preceding paper. For low-density plasmas, the calculations involved trajectory studies of isolated ions in quadrupole-dipole fields with or without fringe fields. For high-density plasmas, two-dimensional particle-in-cell trajectory studies were used to self-consistently incorporate space-charge effects into the simulated plasma behavior in perfect quadrupole-dipole fields uncomplicated by fringe fields. Three aspects of the interaction of the plasma with the radiofrequency fields were investigated: (1) the effects of fringe fields, especially on the injection of the plasma into the quadrupole-dipole field, (2) confinement by and transmission of the flowing plasma through a quadrupole field, and (3) mass-sensitive ejection of ions from the plasma by superimposed quadrupole and dipole fields. For each of these three topics, the theoretical results were compared to the experimental observations, especially in regards to the effect of increasing plasma density. In general, the agreement between theory and experiment is good. The theoretical calculations suggest a limiting current of several hundred microamperes that can be transmitted by the mass filter. The limit is reached when the plasma density increases to the level where the plasma frequency is comparable to the applied rf quadrupole frequency. At higher densities, successive layers of the plasma peel off and are driven out by the applied field until the limiting density is reached. This effect interferes with mass-sensitive ion ejection by the applied dipole field and also induces additional plasma loss in fringe fields. Furthermore, since the dipole frequency is much lower than the quadrupole frequency, it is consequently much reduced from the plasma frequency near the limiting currents. As a result, the applied dipole field has difficulty penetrating the plasma, which leads to significant degradation of mass resolution.

PACS numbers: 52.55.Mg, 52.65. + z, 52.20.Dq,

I. INTRODUCTION

The preceding paper,[1] hereafter referred to as Paper I, reports experimental investigations into the behavior of an ion-pair plasma in the quadrupole-dipole field of a radio frequency (rf) quadrupole mass filter (QMF). The plasma is formed by an efficient electron-transfer reaction in the region of intersection of an intense thermal beam of Cs atoms and an intense supersonic jet of UF_6 molecules. The QMF employed was designed to confine the plasma while at the same time permitting mass-sensitive ejection of ions from the plasma. Operation of the QMF in the ion-ejection mode was selected for this purpose. It was expected that the use of a quasi-neutral plasma would permit far greater throughput than could be obtained under space-charge-limited conditions.

In this paper, companion theoretical studies are reported which allow a greater analysis and interpretation of the experimental results than that presented in Paper I. This paper will include a review of the basic theory[2] of a radiofrequency QMF operated in the ion-ejection mode, trajectory studies designed to simulate the behavior in the QMF of low-density plasmas, and trajectory studies self-consistently incorporating space-charge effects designed to simulate high-density plasma behavior. Both perfect QMF fields and QMF fringe fields are considered. The simulations are constructed so as to produce results directly comparable to the experimental results of Paper I. Not included in this paper is any study of collision dynamics on a molecular level. In particular, there is only a minimal discussion of the electron-transfer reaction[3] of Cs and UF_6 in regards to the initial conditions of the plasma, and there is no consideration of potentially deleterious reactions such as recombination of Cs^+ and UF_6^- or electron exchange of UF_6^- with background neutral UF_6 molecules. These latter reactions are only of importance at much higher plasma densities than those studied experimentally in Paper I.

As will soon become clear, it is impractical to simulate the behavior of the plasma, especially at high density, under fully realistic experimental conditions. All the calculations presented here are highly idealized models of the actual experiments. As a result, there are some noticeable differences between the measured and calculated plasma properties. Nonetheless, taken together, the experimental and theoretical studies present a generally consistent picture of ion-pair plasma behavior in a QMF.

There have been a number of theoretical studies[2,4–10] of ion behavior in a QMF with[9,10] and without [2,4–8] fringe fields. Much of this work has been reviewed by Dawson and Whet-

[a)] Work performed under the auspices of the Office of Basic Energy Sciences, Division of Chemical Sciences, U.S. Department of Energy, under Contract W-31-109-Eng-38.

 0021-8979/83/041755-26$02.40

ten.[2] Almost none of the work incorporates space-charge potentials and so relates only to the behavior of low-density plasmas. Although the studies reported here will reveal no new aspects of ion behavior at low density, certain simplifications in the theory unnoticed by previous investigators will be exploited in analyzing the results. For the higher density plasma calculations, the incorporation of space-charge potentials into the ion trajectories was accomplished by the well-known particle-in-cell method.[11] However, to our knowledge, an ion-pair plasma composed of ions as heavy as Cs^+ or UF_6^- has not previously been studied at this level of simulation.

The outline of this article is as follows. Sections II, III, and IV present calculations of Cs^+-UF_6^- behavior in the QMF with only the quadrupole field applied. Section II involves results at low density where space-charge forces are unimportant. Section III discusses results at high densities where space-charge forces are quite significant. Section IV discusses fringe-field effects which bear on the sensitivity of plasma confinement to the manner of plasma formation. Sections V and VI present calculations of Cs^+-UF_6^- behavior at both low and high density, respectively, in the QMF with both an applied quadrupole and dipole field. Section VII summarizes the results.

II. LOW-DENSITY PLASMA CONFINEMENT AND TRANSMISSION IN QUADRUPOLE FIELDS

A. Brief review

The theory of the behavior of ions in pure quadrupole fields is well known[2,4–10] for ion densities low enough that space-charge forces are insignificant. This theory is fully described in a review by Dawson and Whetten.[2] The pertinent features of the theory are described below, followed by application of the theory to the calculation of Cs^+-UF_6^- behavior in the QMF that can be directly compared to measurements discussed in Sec. V of Paper I.

The electric potential generated by a perfect quadrupole field has the general form

$$V = [U - V_1 \cos(2\pi\nu_1 t)]\,\frac{x^2 - y^2}{2r_0^2}, \tag{1}$$

where the x and y axes are perpendicular to the axis of a QMF characterized by a rf quadrupole voltage of frequency ν_1 and peak-to-peak amplitude at the poles of V_1, a dc potential $U/2$, and a field radius r_0 (the closest distance between two opposite poles is $2r_0$). Consequently, the equation of motion for an ion of charge $\pm e$ and mass m is

$$\frac{d^2x}{d\xi^2} \pm (a_x - 2q_x \cos 2\xi)x = 0, \tag{2}$$

where

$$\xi = \pi\nu_1 t, a_x = \frac{4eU}{m(2\pi\nu_1)^2 r_0^2}, q_x = \frac{2eV_1}{m(2\pi\nu_1)^2 r_0^2}. \tag{3}$$

A similar equation exists for motion in y with a sign change for a_y and q_y. Solutions that describe bounded oscillatory motion exist for only certain regions of a and q, and have the general form

$$x(\xi) = \sum_{s=-\infty}^{\infty} C_{2s}\{\alpha_{\rm I} \cos[(2s+\beta)\xi] + \alpha_{\rm II} \sin[(2s+\beta)\xi]\}, \tag{4}$$

where $\alpha_{\rm I}$ and $\alpha_{\rm II}$ are constants adjusted to the two initial conditions, and C_{2s} and β are functions of a and q. The relationship between β and a and q is in general complicated, but in the limit of a equal to zero and q small, the relationship has the simple and useful form

$$q = \sqrt{2}\beta(1 - \tfrac{1}{8}\beta^2). \tag{5}$$

The dominant term in Eq. (4) as q and a grow small is the term for $s = 0$ and the associated frequency is called the fundamental frequency ν_f, which has the form

$$\nu_f = \frac{\beta}{2}\nu_1. \tag{6}$$

The application of this theory to Cs^+-UF_6^- behavior begins with the stability diagram shown in Fig. 1. This diagram maps out in $|a|$ and $|q|$ the major region corresponding to bounded motion in both x and y directions. The shape of the stability region determines the usual manner in which the QMF is operated as a mass filter. Since a and q are inversely proportional to mass, adjustment of U and V_1 can place the desired mass inside, and all other masses outside, the very "tip" of the stability diagram, resulting in confinement and transmission of only the desired mass. This method of mass filtering will not work for a plasma, which effectively shields out applied d.c. fields from its interior by establishing a charge imbalance at its edges. Thus for a plasma, a QMF will operate effectively only along the base of the stability region in Fig. 1, where $U = 0$. Along the base line, a UF_6^- ion falls outside the stability diagram only if the much lighter Cs^+, with a correspondingly much larger value of q, is far outside the stability diagram. Consequently, the applied fields used to separate the ions would strongly and rapidly promote plasma destruction. As described in Sec. V, a superior manner of operating the mass filter is under conditions where both the UF_6^- and Cs^+ are well within the stability diagram, but where a weak auxiliary field is applied which ejects UF_6^- by resonating with one of the discrete

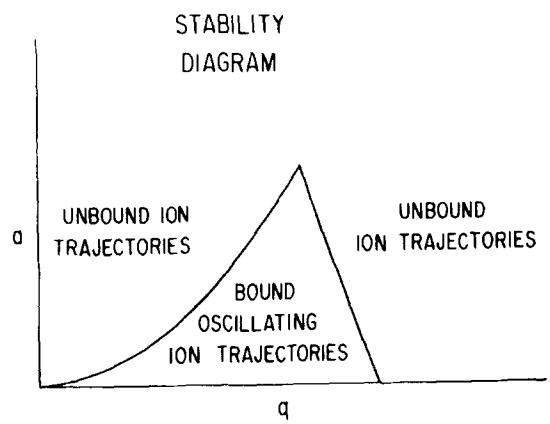

FIG. 1. Stability diagram for stable ion motion in a quadrupole mass filter. a and q are defined in Eq. (3).

number of mass-sensitive frequencies that characterize bound-ion motion in Eq. (4). Because this method of mass filtering was employed, considerable effort was directed to achieving stable plasma confinement in the mass filter.

According to the stability diagram, for $a_x = 0$ at a large enough value of V_1, the fraction of input ions transmitted will be zero. At $q_x = 0$, i.e., no quadrupole field, the initial beam of ions entering the QMF will spread in straight-line trajectories. If the initial velocity in the x or y direction is large enough, a portion of the beam will be lost by intersection with the poles of the mass filter, and the transmitted fraction will consequently be less than one. At values of V_1 between these two extremes, the perfect quadrupole field will induce bound oscillatory motion, whose amplitude depends both on V_1 and the initial conditions [Eq. (4)], and thus the transmitted fraction may vary with V_1 for different initial conditions. Experimentally, the measurement of transmitted flux as a function of V_1, hereafter referred to as a confinement curve, was the major method of experimentally characterizing plasma confinement and transmission in the QMF. Such measurements were made for various initial conditions, in particular, variations of the output flux. The calculation of a confinement curve at low densities consisted of determining the fraction of transmitted trajectories according to Eq. (4) for a statistically significant number of ions in an appropriate initial distribution.

Because the forces determining the trajectory have no component along the axis of the QMF (if fringe fields are ignored), a distribution of ions in the x,y plane will move together if all ions have the same axial velocity. If the distribution can be characterized by only a few parameters, the variation of these few parameters with time, i.e., parameter trajectories, permits rapid calculation of all the properties of ion motion in the QMF. In addition, the form of the distribution and its variation with time persists to some degree at high-ion densities (where space-charge forces operate) and in fringe fields (where forces in the z direction are present), and so are valuable in the interpretation of the results in the following sections. In what follows, the circumstances under which a few parameter trajectories characterize all ion motion will be detailed. Then application of this approach to the calculation of confinement curves will be made. The calculated results will then be compared to the experimental measurements of Paper I.

B. Parameter trajectories

Consider the following rather general set of initial conditions. Let all the ions of one mass enter the QMF in an elliptic distribution centered on $x_c(t_0),y_c(t_0)$ with axes $a(t_0)$ and $b(t_0)$, i.e., the edge of the distribution is initially defined by

$$\left[\frac{x(t_0)-x_c(t_0)}{a(t_0)}\right]^2+\left[\frac{y(t_0)-y_c(t_0)}{b(t_0)}\right]^2=1. \tag{7}$$

Let the off-axis velocity of each ion in the initial distribution be the sum of the velocity of the center of the distribution plus a velocity directly proportional to the displacement of the ion from the center of the distribution, i.e.,

$$\begin{aligned}\dot{x}(t_0)&=\dot{x}_c(t_0)+\frac{x(t_0)-x_c(t_0)}{a(t_0)}\dot{a}(t_0)\\ \dot{y}(t_0)&=\dot{y}_c(t_0)+\frac{y(t_0)-y_c(t_0)}{b(t_0)}\dot{b}(t),\end{aligned} \tag{8}$$

where

$$|\dot{x}_c(t_0)|+|\dot{a}(t_0)|$$

and

$$|\dot{y}_c(t_0)|+|\dot{b}(t_0)|$$

are the maximum velocities in the x and y directions, respectively. If the velocity of each ion along the axis of the QMF is constant, then these initial conditions and the homogeneous nature of Eq. (2) allow $x(t)$ and $y(t)$ to be written as

$$\begin{aligned}x(t)&=x_c(t)+\frac{x(t_0)-x_c(t_0)}{a(t_0)}a(t)\\ y(t)&=y_c(t)+\frac{y(t_0)-y_c(t_0)}{b(t_0)}b(t),\end{aligned} \tag{9}$$

where $x_c(t),y_c(t),a(t)$, and $b(t)$ satisfy Eq. (2) with initial conditions $x_c(t_0),\dot{x}_c(t_0)$, etc. Furthermore, because of Eq. (7), a rearrangement of Eq. (9) shows that

$$\left[\frac{x(t)-x_c(t)}{a(t)}\right]^2+\left[\frac{y(t)-y_c(t)}{b(t)}\right]^2=1. \tag{10}$$

The distribution in the x,y plane according to Eq. (10) remains elliptical with time-varying parameters $x_c(t),y_c(t)$, $|a(t)|$, and $|b(t)|$. Thus the calculation of a large number of individual-ion trajectories can be replaced by the calculation of only four parameter trajectories. Furthermore, if the distribution is initially centered on the axis such that

$$x_c(t_0)=y_c(t_0)=\dot{x}_c(t_0)=\dot{y}_c(t_0)=0,$$

the distribution will always be centered on the axis, and only $a(t)$ and $b(t)$ need to be followed. Of course, the parameter trajectories have the same analytic solution as that previously discussed for individual-ion motion, namely, Eq. (4).

C. Calculated confinement curves

The actual calculation of a confinement curve for comparison with experiment consists of determining the transmitted fraction of the initial distribution. With the assumption that any ion that touches the poles of the QMF will be lost, the transmitted fraction is most conveniently calculated from the nontransmitted fraction, which is measured by the overlap of the distribution with the hyperbolic pole structure during the transit time of the ions in the mass filter. Since different portions of the distribution can overlap the pole structure at different times, and since the same portion of the distribution can overlap the pole structure many times, the nontransmitted fraction must be continuously monitored, without multiple counting, during the propagation of the distribution through the mass filter.

To perform the calculation, an initial distribution appropriate for the experimental situation must be formulated. In the experiments, the plasma is created by an electron-

transfer reaction of an accelerated jet of UF_6 molecules directed along and centered about the axis of the QMF. If the slight off-axis shift caused by the thermal Cs beam is ignored, the initial distribution of ions in the plane perpendicular to that axis should be circular and centered in the axis, i.e.,

$$\begin{aligned} &x_c(t_0) = y_c(t_0) = \dot{x}_c(t_0) = \dot{y}_c(t_0) = 0 \\ &a(t_0) = b(t_0) \equiv R_0 \\ &\dot{a}(t_0) = \dot{b}(t_0) \equiv v_\perp , \end{aligned} \tag{11}$$

where R_0 and $v_\perp$ are the maximum radius and spreading velocity of the UF_6 beam, respectively. As mentioned earlier, these conditions guarantee that the distribution will remain centered during the transit time or $x_c(t) = y_c(t) = 0$. For $a(t)$ and $b(t)$, R_0 and $v_\perp$ must be selected.

To determine the range of R_0 and $v_\perp$ consistent with the experiments, both the actual geometry and the collision dynamics have to be considered. Because of considerable variation in experimental arrangements, the values of R_0 sampled by the experiments, considering only geometric constraints, range over an order of magnitude, from 0.25 to 2.5 cm. $v_\perp$ can then be determined by dividing the value of R_0 by the transit time from the beam source to the QMF entrance. Given the experimental geometry and the $Cs^+ + UF_6^-$ center-of-mass velocity of 1.4×10^5 or 1.75×10^5 cm/sec (UF_6 seeded in He or H_2, respectively; see Sec. IV of Paper I), the range of $v_\perp$ under geometric constraints alone is 0.01×10^5 to 0.6×10^5 cm/sec.

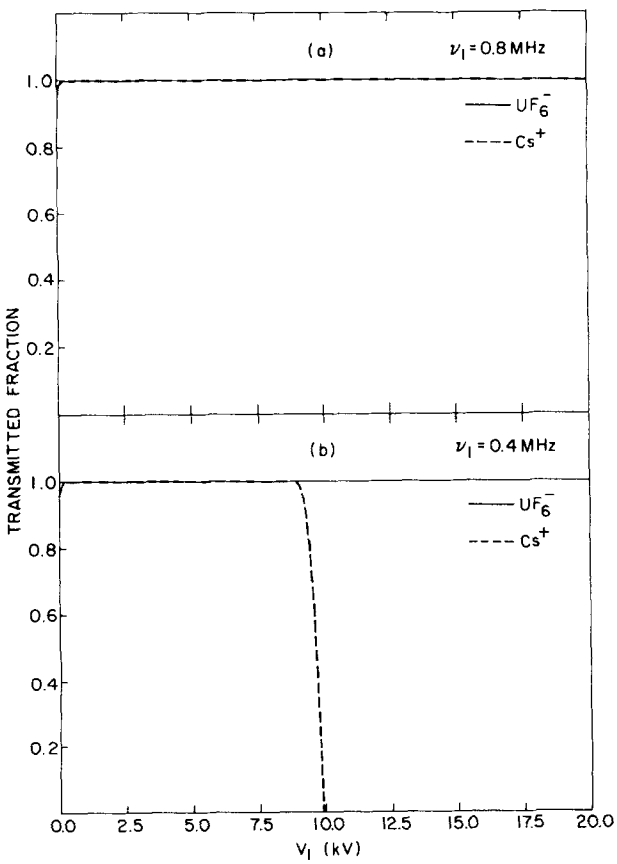

FIG. 2. (a) Confinement curves for UF_6^- (solid line) and Cs^+ (dashed line) calculated from low-density theory for $\nu_1 = 0.8$ MHz. The initial radius R_0 is 1.0 cm and the initial off-axis velocity $v_\perp$ is 10^4 cm/sec; (b) as in (a) for $\nu_1 = 0.4$ MHz.

These ranges of values for R_0 and $v_\perp$ ignore the fact that under the experimental conditions, the electron-transfer reaction releases a relative energy[12] of about 1.6 or 2.9 eV (UF_6 seeded in He or H_2, respectively). How this energy is distributed among translational or internal degrees of freedom (including electronic[3]) is not known. How the translational energy is distributed among the axial and off-axial degrees of freedom is also not known. In the extreme case that all the energy appeared in off-axis translational motion, then $v_\perp$, especially for Cs^+, could become comparable to the axial velocity ($\gtrsim 1.5\times10^5$ cm/sec). This extreme case is highly unlikely. The cross section of 175 Å^2 at a relative energy of 2.9 eV (see Sec. IV of Paper I) suggests that the electron-transfer reaction is dominated by large impact-parameter (> 7 Å) collisions that produce only small-angle deflections of UF_6^-. It is likely that whatever translational energy is released will be as axial translational energy, which does not influence $v_\perp$ directly. At high enough plasma density, space-charge effects would couple all the translational degrees of freedom, but this complication will be discussed in the next two sections. For low-density plasmas discussed here, the collision dynamics probably does not alter significantly the range of R_0 and $v_\perp$ selected from geometric constraints alone.

The only remaining specification that must be made prior to the calculation of confinement curves is the value of the initial time t_0, which through Eq. (1) is in effect the initial phase of the field, and can be expressed as a fraction of the period, $1/\nu_1$, of the quadrupole field. The experiments always measure phase-averaged values, and therefore phase averaging must be done numerically for direct comparison with the measurements.

Figure 2(a) displays the calculated phase-averaged confinement curves for both UF_6^- and Cs^+, as calculated by the low-density theory for a perfectly aligned plasma beam with $R_0 = 1.0$ cm, $v_\perp = 0.1$ km/sec, and $\nu_1 = 0.8$ MHz. The confinement is seen to be perfect for V_1 from about 0.25 to above 20 kV for both ions at this quadrupole frequency. Increasing R_0 to 3 cm, varying $v_\perp$ from 0 to 1 km/sec, or introducing misalignment up to 1 cm does not alter the confinement curve above $V_1 = 1$ kV. These results indicate that the actual experimental arrangement and operating parameters (see Sec. III of Paper I) have been properly selected to achieve the desired goal of perfect plasma confinement, at least at low density.

Figure 2(b) records the analogous confinement curves for UF_6^- and Cs^+ with $\nu_1 = 0.4$ MHz. Similar to $\nu_1 = 0.8$ MHz, the confinement for UF_6^- is perfect for V_1 from approximately 1 kV to beyond 20 kV. However, unlike the results for $\nu_1 = 0.8$ MHz, the Cs^+ confinement rapidly declines for V_1 beyond 7 kV, and ceases altogether for V_1 greater than 10 kV. Reasonable variations of the initial size and off-axis velocity of the ion distribution does not qualitatively change these results. Cs^+ is not confined at high values of V_1 because the low value of ν_1 places Cs^+ out of the region of stability for $V_1 \gtrsim 10$ kV (see Fig. 1).

Although the distribution of ions as a function of time in the QMF was not directly measurable in any of the experiments, such distributions illustrate several basic concepts, and form a base line for analyzing the high-density plasma calculations to be discussed in the next section. For the initial conditions used in Fig. 2, the x axis of the elliptic distributions of UF_6^- and Cs^+ is plotted as a function of time in Fig. 3 for $V_1 = 16.5$ kV and for zero initial phase of the field. Only the values for the first 48 μsec of the transit time are shown. Consider first Fig. 3(a), for $\nu_1 = 0.8$ MHz. Note that the oscillations of the ellipse axis of UF_6^- are predominantly at the single frequency of ~ 0.04 MHz, while the Cs^+ axis oscillates with one major but several strong minor frequencies, all of which are noticeably higher than 0.04 MHz. Because q is inversely proportional to mass and therefore smaller for UF_6^- than for Cs^+, the fundamental frequency [see Eqs. (5) and (6)] is both smaller and more dominant for UF_6^- than for Cs^+. On a finer scale than that of Fig. 3, isotopes of either ion would have slightly different fundamental frequencies, a fact that can be exploited for isotope separation, as will be discussed later. Note also that the maximum size of the axis for either ion distribution never exceeds by 50% the initial value of 1.0 cm. However, the minimum size of the axis actually shrinks to zero at regular intervals. If space-charge forces were included in the theory, such drastic shrinkage could not occur.

Figure 3(b) displays the results for $\nu_1 = 0.4$ MHz. The oscillations of the UF_6^- distribution are still dominated by the fundamental frequency, although other higher frequencies are quite pronounced because q is larger. The fundamental frequency is ~ 0.08 MHz, twice that for the case of $\nu_1 = 0.8$ MHz, as expected from Eqs. (5) and (6). (The separation in frequencies for the two uranium isotopic ions has also increased by a factor of 2.) The Cs^+ distribution almost immediately exceeds the dimensions of the QMF, graphically illustrating unbounded motion outside the stability diagram (Fig. 1). Note also that the axis of the ellipse of the UF_6^- distribution periodically more than doubles its initial value, indicating that UF_6^- also is less tightly confined at $\nu_1 = 0.4$ MHz than at $\nu_1 = 0.8$ MHz.

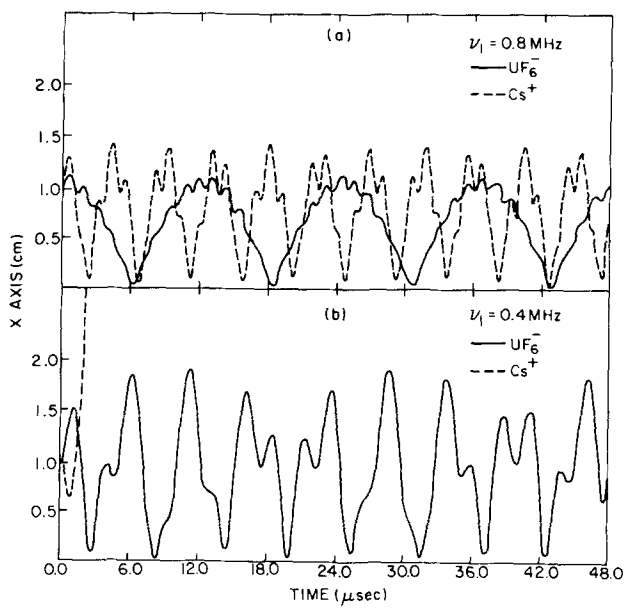

FIG. 3. (a) x axis of the elliptic distributions of UF_6^- (solid curve) and Cs^+ (dashed curve) as calculated by low-density theory for $V_1 = 16.5$ kV, $\nu_1 = 0.8$ MHz, $R_0 = 1.0$ cm, $v_\perp = 10^4$ cm/sec, and zero initial phase of the field; (b) as in (a) for $\nu_1 = 0.4$ MHz.

D. Comparison to experimental measurements

The shapes of the confinement curves in Fig. 2 agree well with those of the lowest density measured curves for $\nu_1 = 0.8$ MHz as shown in Figs. 6, 7, and 9 in Paper I. However, as can be seen in the same three figures, at higher densities the measured confinement degrades at higher values of V_1. This loss of confinement can be significantly affected by fringe and extraction fields at the ends of the QMF which are present in the experiment but not in the above calculation. If the plasma is formed in the entrance fringe field outside the QMF, as in the crossed-beam injection mode, then the loss of confinement at high V_1, as seen in Fig. 9 of Paper I, is much more severe than that shown in Figs. 6 and 7 in Paper I for the merged-beam mode, where the plasma forms within the QMF. (For a description of the two modes of plasma formation, see Sec. IV of Paper I.) If the strength of extraction fields at the exit of the QMF is increased, the loss of confinement at high V_1 is significantly reduced, as seen in Fig. 8 of Paper I. Thus, at high plasma densities, the experimental shape of the confinement curves deviates from that calculated in the low-density limit primarily due to effects at the ends of the QMF and, at the highest densities, perhaps due to effects within the QMF.

For $\nu_1 = 0.4$ MHz, the calculated Cs^+ confinement curve in Fig. 2 is very similar to the measured curves at all densities, as seen in Fig. 12 of Paper I. The only qualitative difference is the persistence of some slight Cs^+ confinement at high values of V_1 as the density increases. However, the calculated UF_6^- confinement curve in Fig. 2 does not have the break at $V_1 = 10$ kV that all the measured curves show, as seen in Fig. 13 of Paper I. The lowest densities measured for $\nu_1 = 0.4$ MHz are more than one order of magnitude higher than those studied for $\nu_1 = 0.8$ MHz and as will be shown in the next section, the break is probably an effect of space-charge forces.

III. HIGH-DENSITY PLASMA CONFINEMENT AND TRANSMISSION IN QUADRUPOLE FIELDS

At the highest plasma densities studied experimentally, space-charge forces would be expected to be important and could perhaps account for the discrepancies between the low-density theoretical results and the actual experimental measurements. Consequently, particle-in-cell (PIC) trajectory[11] studies of plasma behavior inside the QMF were carried out. These studies explicitly include space-charge forces within the context of a trajectory calculation, and they produce many qualitative features of the experimental results which appear under high throughput conditions. In what follows, several plasma parameters for the experimental conditions will be listed, then the PIC technique and its application to calculating plasma behavior in the QMF will be de-

scribed, and finally the calculated results for plasma confinement will be presented.

A. Plasma parameters

In Table I, the plasma density ρ, frequency ν_p, Debye shielding length λ_D, and collision frequency ν_c are listed as a function of the positive or negative ion current I, the plasma radius R_0, and the average internal relative velocity $\langle v \rangle$. The two values of I—40 and 400 μA—bracket the highest measured output current of ~ 300 μA and span the range of currents where space-charge effects are obvious in the experimental record. The two values of R_0—1 and 3 cm—bracket the higher value of R_0 derived from geometric constraints in the previous section. The lowest value of $\langle v \rangle$ is half the 1.75×10^5 cm/sec center-of-mass velocity of $Cs^+ + UF_6^-$ for UF_6 accelerated in H_2. This value would be typical for a plasma whose internal energy comes primarily from the relative energy of the chemi-ionization collision (see Sec. II C). The higher values of $\langle v \rangle$ correspond to a plasma whose internal energy comes from the time-varying applied field. If that field induces sinusoidal oscillations in the relative motion whose amplitude is R_0 and whose frequency is the fundamental frequency, then the higher values of $\langle v \rangle$ in the table are the root-mean-square velocity for this motion when $\nu_1 = 0.8$ MHz.

The current I, the radius R_0, and the axial velocity (assumed to be 1.75×10^5 cm/sec) is all that is required to calculate the density ρ. These densities are about a factor of 2 less than the maximum measured density of 1.1×10^{10} cm^{-3} in the crossed-beam intersection region in front of the QMF entrance. The plasma frequency ν_p is given by

$$\nu_p = \frac{1}{2\pi}\left(\frac{4\pi e^2}{\mu}\rho\right)^{1/2}, \tag{12}$$

where μ is the reduced mass for $Cs^+ + UF_6^-$ motion. The plasma frequency ranges from five times less to two times greater than the frequency of the applied field for $\nu_1 = 0.8$ MHz. The Debye shielding length λ_D is given by

$$\lambda_D = \left(\frac{kT}{4\pi e^2 \rho}\right)^{1/2} = \frac{\langle v \rangle}{2\sqrt{3}\pi \nu_p}, \tag{13}$$

where T is the temperature for average internal relative ion motion, k is the Boltzman constant, and kT is assumed to be related to $\langle v \rangle$ by

$$\tfrac{3}{2} kT = \tfrac{1}{2} \mu \langle v \rangle^2. \tag{14}$$

The values of λ_D vary by a factor of 40 and are small relative to the dimensions of the plasma or the QMF. Finally, the collision frequency is determined by

$$\nu_c = \langle v \rangle \rho \sigma, \tag{15}$$

where σ is the collision cross section whose value was set at 100 Å^2 to calculate ν_c for the table. The density ρ used to calculate ν_c is the plasma density and ignores the un-ionized UF_6 beam that also enters the QMF. Even if only 1% of the neutral beam undergoes chemi-ionization (5% is a better experimental estimate), the resulting ν_c, increased by two orders of magnitude from the table values, is still equivalent to less than one collision per transit time of the QMF. Thus the plasma is essentially collision-free.

The values listed in Table I indicate that at the higher currents studied experimentally, the Cs^+- and UF_6^--ion distributions will exhibit collective plasma behavior. The plasma will resist penetration by d.c. fields because λ_D is small. The plasma will allow penetration of the rf quadrupole fields, although with some difficulty at the highest densities where ν_p is larger than ν_1. The plasma density is low enough to be collision-free and is several orders of magnitude lower than typical dense electron-ion plasmas.

B. Particle-in-cell model

In the PIC trajectory model,[11] all trajectories are followed simultaneously. After each time step, a charge distribution is obtained from the ion positions; Poisson's equation is solved numerically for this charge distribution and the appropriate boundary conditions. The resulting space-charge potential is used in conjunction with the applied electrical potential to supply the forces which advance the trajectories over the next time step. Since the motion of charged particles in electric fields does not depend on the absolute values of their masses or charges but only the ratio of the charge to mass, only the trajectories of a finite number of fictitious super-heavy, super-charged simulation particles of the right e/m ratio are calculated. To obtain a charge distribution from the positions of a finite number of simulation particles, the region over which Poisson's equation must be solved is subdivided into equal units or cells fixed in space. The charge carried by a simulation particle is assumed to be uniformly distributed over a cell-sized region centered on the simulation particle. The overlap of the region of charge for each simulation particle with the cellular regions fixed in

TABLE I. Plasma parameters of density ρ, frequency ν_p, Debye shielding length λ_D, and collision frequency ν_c as a function of current I, plasma radius R_0, and average internal relative velocity $\langle v \rangle$.

I (μA)	R_0 (cm)	$\langle v \rangle$ (10^5 cm/sec)	ρ (10^9 cm^{-3})	ν_p (MHz)	λ_D (cm)	ν_c (Hz)
40	1.0	0.875	0.45	0.46	0.0176	0.4
		3.554	0.45	0.46	0.0716	1.6
	3.0	0.875	0.05	0.15	0.0529	0.04
		10.663	0.05	0.15	0.6450	0.2
400	1.0	0.875	4.54	1.44	0.0056	4.0
		3.554	4.54	1.44	0.0226	15.8
	3.0	0.875	0.50	0.48	0.0167	0.4
		10.663	0.50	0.48	0.2041	1.8

space results in a spatially discretized charge distribution represented by the net accumulated charge in each cell. For two-dimensional square or rectangular charge distributions with simple boundary conditions, the solution to Poisson's equation can be rapidly obtained by fast Fourier transform techniques.[13,14] Given the resulting discretized space-charge potential at each cell center as well as the applied potential, the force on each simulation particle can be determined by first-order differences, and the particle can be advanced by the central difference form of Hamilton's equations.

Since the PIC simulation is only practical for a two-dimensional model with square or rectangular boundaries, the technique can only be applied to a highly idealized model of plasma behavior in the actual QMF. While the perfect quadrupole potential of Eq. (1) has only two dimensions, the x and y off-axis coordinates, ion density varies as a function of z because ions entering the QMF at different times experience different phases of the applied field. At low ion density, this variation generates a negligible space-charge force in the z direction, and ions entering the QMF at one time can be followed in two spatial dimensions as a function of time, independent of ions entering the QMF at any other time. At high ion density, axial space-charge forces are significant, and the full simulation must involve three spatial dimensions. To reduce the simulation to two dimensions, the initial conditions were modified so that the plasma is assumed to form instantaneously and uniformly throughout the whole length of the QMF. The plasma is assumed to have no axial velocity, but it is followed in time only over the transit time of the actual plasma in the QMF. The QMF is assumed to have no fringe fields at its ends. With these assumptions, there can never be any axial variations of ion density. An additional idealization in the model is to assume that the space-charge potential goes to zero on an axially square boundary of dimensions $2r_0 \times 2r_0$ in the xy plane and that ions reaching the boundary are lost. The actual hyperbolic boundary about each of the four poles does not permit a practical solution to Poisson's equation.

Given this idealized model, the accuracy and expense of the computed solution depends on three critical parameters. They are the time step Δt over which the trajectories are advanced, the number of simulation particles N_p, and the number of square cells, $N_c \times N_c$, that fill up the area enclosed by the square boundary. The larger Δt and the smaller N_p and N_c, the less expensive but also the less accurate the calculation. The physical considerations and numerical tests used to select the values for these parameters are detailed in Appendix A. The final values make the calculations feasible but produce only qualitative to semiquantitative accuracy.

For almost all the simulations presented here, only two input currents were examined: 40.3 and 403 μA (assuming an axial velocity of 1.75×10^5 cm/sec appropriate for the merged-beam experiments with UF_6 accelerated in H_2). For all simulations, the plasma was initially uniform, cylindrical, and centered on the QMF axis. Because of the symmetry of these initial conditions and of the applied field, only particles initially in one quadrant need be followed, for reflection symmetry at any time can recreate the entire charge distribution necessary for the derivation of the space-charge potential. This in fact was done, at great savings in computational expense. For almost all the simulations, the initial radius of the plasma, R_0, was 2 cm, the initial maximum off-axis velocity, $v_\perp$, was 0.316×10^5 cm/sec, and the initial phase of the field was zero. Additional calculations indicate that reasonable variations in $v_\perp$ have a minor effect; phase averaging a 10% effect; and 1-cm variations in R_0 no qualitative effect on calculated confinement curves.

In the next two parts of this section, calculated confinement curves and the mechanism of plasma loss for $\nu_1 = 0.4$ MHz and for $\nu_1 = 0.8$ MHz are discussed separately. Both the PIC results and a simpler model of space-charge effects will be used in the discussion. The calculations suggest an upper bound to the transmitted current which is explored in more detail in the last part of this section.

C. Results and analysis for $\nu_1 = 0.4$ MHz

1. Results

For $\nu_1 = 0.4$ MHz, the calculated confinement curves for both UF_6^- and CS^+ are displayed in Fig. 4 for variations in input current. The curves are straight-line segments connecting the calculated output current at specific values of V_1. The confinement curves are for a simulation time of only 60 μsec, or 10.5% of the full experimental transit time (assuming 1.75×10^5 cm/sec axial velocity). For $V_1 \geqslant 5$ kV, extrapolation from several calculations for a 120-μsec simulation time indicates the confined current in Fig. 4 will drop by less than 10% for the full transit time. However, for $V_1 = 0$, the final transmitted current will be only $\sim 35\,\mu$A for an input current of 403 μA. This is a consequence of the initial radial velocity of the plasma which is unchanged in the absence of a field. As will be discussed later, the mechanisms of plasma loss are the same for all values of V_1 (except very near $V_1 = 0$), but take longer to develop for the lower values of V_1. From these considerations and extrapolations from other calculations, the calculated maximum final transmitted current is expected to be $\sim 150\,\mu$A at $V_1 \approx 2.5$ kV.

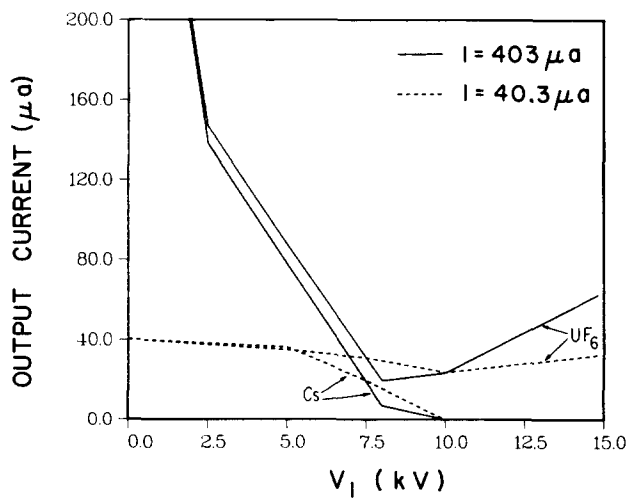

FIG. 4. Confinement curves for UF_6^- and Cs^+ calculated with the PIC model for $I = 403\,\mu$A (solid curve) or 40.3 μA (dashed curve) and $\nu_1 = 0.4$ MHz. The simulation time is 10.5% of the transit time.

The Cs^+ results in Fig. 4 show a rapid decrease in the confinement curve as V_1 approaches 8–10 kV. Above 10 kV, no Cs^+ is confined, but a fraction of the UF_6^- remains confined and that fraction increases as V_1 increases. The Cs^+ results agree with both experimental measurements (Fig. 12 of Paper I) and low-density theoretical calculations [Fig. 2(b)]. Clearly, space-charge effects do not oppose the applied field. If anything, the calculated Cs^+ results are in better agreement with the experimental measurements than are the low-density calculations in that a greater loss of Cs^+ occurs at lower values of V_1 [see Figs. 2(b) and 4, and 12 of Paper I].

The UF_6^- results in Fig. 4 show a break in the confinement curve at the values of V_1 where Cs^+ loss is essentially complete. This is in better agreement with experimental results (Fig. 13 in Paper I) than is low-density theory which has no break. However, the shape of the experimental confinement curves appears to qualitatively change with increased density in a manner different from that in Fig. 4. As explained in Paper I, the change in shape is primarily due to space-charge effects in the extraction region outside the QMF. If the effects are taken into account, the evidence suggests that the confined current within the QMF is qualitatively similar to the calculations in Fig. 4. However, on a more quantitative level, two differences can be seen. First, the calculated confinement curves at high V_1 increase with V_1 while the experimental curves do not. Second, the calculated decline in confinement as V_1 approaches ~ 10 kV is relatively small at currents of 40 μA, but is experimentally significant at currents as low as 1 μA.

2. Analysis

These two differences occur under conditions where the plasma exists for only a short time in QMF before rapid Cs^+ loss reduces it to a UF_6^- distribution. The behavior of such a single-charge distribution in the presence of space-charge forces can be calculated by a model that is more approximate than the PIC model, but is also more easily interpreted and analytic (and thus free from any question of numerical accuracy). This model will be called the uniform cylindrical charge (UCC) model and it will form the basis of understanding space-charge effects without the complications of collective plasma behavior. The UCC model is exactly like the PIC model for a single-charge distribution with two exceptions. First, the perfect quadrupole potential is approximated by a radial harmonic potential that induces in isolated ions radial oscillations at only the fundamental frequency. Second, the square boundary in the xy plane at which the space-charge potential vanishes and particles are lost is replaced by a circular boundary of radius r_0. As is shown in detail below, these approximations result in analytic ion dynamics, even in the presence of space-charge potentials. The UCC and PIC models produce qualitatively similar results which suggest that the difference between PIC theory and experiment are not due to numerical inaccuracy, but to idealized initial and boundary conditions.

The first step in determining the ion dynamics for the UCC model is to express the initial form of the equations of motion. This requires the initial space-charge potential, V_{sc}, which for the initial uniform cylindrical ion distribution, takes the form, in cylindrical coordinates, of

$$V_{sc}(r,\phi,z) = e(I/\dot{z}_0)\begin{cases} \left(1 - \dfrac{r^2}{R_0^2}\right) + 2\ln(r_0/R_0), r \leqslant R_0 \\ 2\ln(r_0/r), r > R_0 \end{cases}, \quad (16)$$

where I is the initial ion current, $\dot{z}_0$ is the initial (and presumably unchanged) ion axial velocity, R_0 is the initial radius of the ion distribution, and r_0 is the field radius. V_{sc} is clearly independent of polar angle ϕ and axial distance z and so is the applied potential which, as mentioned above, is approximated as radial and harmonic. Given Eq. (16) and the applied potential, Newton's equation for ion motion in ϕ or z is trivial; but, for motion in r, it initially takes the form

$$\ddot{r} + \omega_f^2 r = \frac{2e^2(I/\dot{z}_0)}{m}\begin{cases} \dfrac{r}{R_0^2}, r \leqslant R_0 \\ \dfrac{1}{r}, r > R_0 \end{cases}, \quad (17)$$

where $\omega_f = 2\pi\nu_f$. The second term on the left-hand side is due to the applied potential and would produce radial oscillations in r at ν_f if the space-charge potential (proportional to I) were to vanish.

The second step in determining the ion dynamics is to show that Eq. (17) is not only initially true but true for all time if the initial radius R_0 is replaced by a time-dependent radius $R(t)$. This is equivalent to showing that Eq. (17) preserves the initial radial uniformity of the cylindrical ion distribution, a necessary and sufficient requirement for the space-charge force in Eq. (17) to be valid. A distribution will remain radially uniform if an ion at any radial position $r(t)$ changes position in proportion to the change in the distribution's radius $R(t)$, i.e.,

$$\frac{d[r(t)/R(t)]}{dt} = 0. \quad (18)$$

The initial conditions on the radial velocity of the distribution obey this equation [see Eq. (8)]. Furthermore, Eq. (17) guarantees that if Eq. (18) is initially obeyed, it is always obeyed. In particular, from Eq. (17), it can be shown that the second derivative of $[r(t)/R(t)]$ is proportional to the first:

$$\frac{d^2[r(t)/R(t)]}{dt^2} = -2\left(\frac{dR(t)/dt}{R(t)}\right)\left(\frac{d[r(t)/R(t)]}{dt}\right). \quad (19)$$

But from Eq. (19), it can be shown that all higher derivatives of $[r(t)/R(t)]$ are proportional to the first. Thus, since Eq. (18) is initially true, under Eq. (17) it is always true and the distribution remains radially uniform. Equation (17) is therefore true for all time if $R(t)$ replaces R_0.

The third step in determining the ion dynamics is to develop the relationship between the final transmitted current and the radius of the ion distribution. Since the ion distribution does not depart from being uniform and cylindrical, it can be characterized by only its radius, which from Eq. (17) is given by

$$\begin{aligned} &\ddot{R}(t) + \omega_f^2 R(t) = \frac{2e^2(I/\dot{z}_0)}{mR(t)} \\ &R(0) = R_0 \\ &\dot{R}(0) = v_\perp. \end{aligned} \quad (20)$$

In the absence of space-charge forces, $R(t)$ will experience sinusoidal oscillations at the fundamental frequency. With the inclusion of space-charge forces, $R(t)$ will periodically oscillate between a minimum and maximum value determined by the relative strengths of the applied and space-charge fields. If the maximum in $R(t)$, designated R_{MAX}, exceeds r_0, ions will be lost and the final transmitted current I_{OUT} will be reduced from the input current I according to

$$I_{OUT} = \text{MIN}\left\{1, \frac{r_0^2}{R_{MAX}^2}\right\} I. \tag{21}$$

The final step in determining the ion dynamics is to obtain an algebraic equation for R_{MAX} and hence I_{OUT}. With the relation

$$\ddot{R}(t) = \frac{1}{2}\frac{d\dot{R}(t)}{dR(t)}, \tag{22}$$

the second-order differential equation for R as a function of t [Eq. (20)] can be converted into a first-order differential equation for $\dot{R}$ as a function of R. The equation can be integrated and the result, along with the fact that $\dot{R}$ is zero at R_{MAX}, provides a transcendental equation for R_{MAX}:

$$R_{MAX}^2 = R_0^2 + \frac{v_1^2}{\omega_f^2} + \frac{2e^2(I/\dot{z}_0)}{m\omega_f^2}\ln(R_{MAX}/R_0)^2. \tag{23}$$

Equations (23) and (21) therefore determine I_{OUT}.

Table II lists I_{OUT} calculated from the UCC model for $I = 403\ \mu$A, for different values of R_0, and for the higher values of V_1 where Cs^+ is no longer retained. Also listed in Table II are the analogous PIC values of I_{OUT} as displayed in Fig. 4. The table indicates that the UCC model and the PIC calculations are in reasonable accord, especially if one permits a residual effect of the Cs^+ in the form of a larger "effective" initial radius in the UCC model than in the PIC model.

For $I = 40.3\ \mu$A, the UCC model predicts (within 5%) perfect confinement for all entries in Table II. This is also similar to the PIC results in Fig. 4, where confinement loss is not very significant. Thus the PIC model at higher values of V_1 for $\nu_1 = 0.4$ MHz can be thought of in terms of the space-charge-limited transit of a UF_6^- distribution initially made more diffuse by the departing Cs^+.

Both the UCC and PIC models share the two areas of disagreement with experiment discussed earlier, namely, failure to predict loss of confinement for currents as low as 1 μA and failure to predict loss of confinement for higher currents that is independent of V_1. The origin of both of these discrepancies must be due to approximations shared by both the UCC and PIC models. These approximations include the neglect of axial forces of any kind, the unformity of the initial plasma distribution, and the simple boundary conditions. Inasmuch as collection fields strongly influence the shape of the experimental confinement curve, as mentioned previously, the neglect of axial forces in both models is probably a major component in the disagreement with experiment.

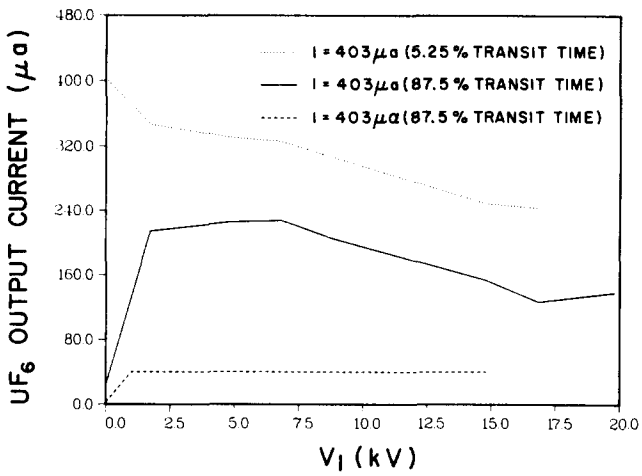

FIG. 5. Confinement curves for UF_6^- calculated with the PIC model for $I = 403\ \mu$A (solid curve, dotted curve), 40.3 μA (dashed curve), and $\nu_1 = 0.8$ MHz. The dotted curve is for a simulation time that is 5.25% of the transit time. The other curves are for a simulation time that is 87.5% of the transit time.

D. Results and analysis for $\nu_1 = 0.8$ MHz

1. Results

With $\nu_1 = 0.8$ MHz, it was shown in Sec. II C that the applied field will perfectly confine both UF_6^- and Cs^+ in the absence of space-charge forces. The effect of space-charge forces is seen in Fig. 5, where the PIC calculated confinement curves for UF_6^- are displayed for input currents of 40.3 and 403 μA. The curves are straight-line segments connecting the calculated output current at specific values of V_1. The solid and dashed confinement curves are for the higher and lower input currents, respectively, for a simulation time that is 87.5% of the full experimental transit time (assuming 1.75×10^5 cm/sec axial velocity). The dotted curve is for the higher input current for a simulation time that is only 5.25% of the transit time. Because of the expense, no PIC calculations were carried out to the full transit time.

The calculated confinement at 40.3 μA is essentially perfect and in accord with all but the highest current experiments with merged-beam injection, which eliminates deleterious entrance fringe-field effects, as will be discussed later. The calculated confinement at 403 μA is not perfect. Losses are about 50% at all values of V_1 and mostly occur in the first 5–10% of the transit time. (For very low values of V_1, the field is too weak to significantly influence the plasma, and

TABLE II. For the UCC and PIC models, I_{OUT} (μA) as a function of both V_1 (kV) and R_0 (cm) for $I = 403\ \mu$A.

R_0 (cm)	1.0			2.0			3.0		
V_1 (kV)	12	14	16	12	14	16	12	14	16
UCC	22	32	44	30	45	64	39	59	86
PIC	49	61		41	56				

losses are primarily a consequence of the initial radial velocity of plasma and not of space-charge effects.) The confinement curve is not flat but declines somewhat at high V_1. The maximum total current confined is $\sim 225\,\mu$A, which is approximately $100\,\mu$A less than the highest value recorded in any of the experiments (Fig. 7 in Paper I). The calculated decline in the confinement curve at high V_1 agrees with experimental measurements. However, the decline could be moderated by extraction and collection voltage (Fig. 8 in Paper I), indicating that it is related to the exit fringe-field conditions. The calculations suggest that part of the decline might also be due to effects strictly within the QMF. The calculated decline is mild compared to the drastic loss in confinement measured at high V_1 and high flux with the crossed-beam injection method, an effect which is due almost entirely to entrance fringe-field effects (to be discussed later).

The calculations displayed in Fig. 5 are only for UF_6^-. The calculated Cs^+ confinement curve for an input current of 40.3 μA is identical to that for UF_6^-. At the high input current of 403 μA, the calculated Cs^+ confinement curve is within 10% of that for UF_6^- and generally lower. The experimental results show Cs^+ and UF_6^- confinement to be quite similar, in accord with the calculations, but with Cs^+ output current slightly higher than that for UF_6^-. However, the measured differences in UF_6^- and Cs^+ output currents were small enough so that they could easily be influenced by phenomena not included in the PIC calculations, such as fringe, extraction, and collection-field effects and asymmetries in the initial plasma distribution.

The major observation to be drawn from the PIC calculations is that, as the plasma density increases, loss of confinement becomes significant in a way that does not qualitatively alter the shape of the confinement curve. In other words, significant loss of confinement occurs at all values of V_1. Both the 40.3- and 403-μA confinement curves in Fig. 5 have roughly the same shape, but confinement is perfect at the lower input current, while the majority of the plasma is lost at the higher input current. The same effect is also seen for $\nu_1 = 0.4$ MHz below $V_1 \approx 10$ kV where a plasma still exists. There is no experimental evidence available to test this prediction because of the difficulty of experimentally distinguishing plasma losses in fringe fields at the entrance or exit of the QMF from plasma losses within the QMF itself, which is all the theory pertains to.

2. Analysis

The mechanism of plasma loss begins with the question of plasma penetration by the applied field. Note that from Fig. 5 substantial plasma loss has occurred in the first 5% of the transit time. Even if the applied field were completely unable to penetrate the plasma, the initial radial energy, characterized by $v_\perp$, would be insufficient to cause any plasma loss in such a short time. In fact, from Table I, the plasma frequency ν_p for the PIC simulations represented in Fig. 5 is always less than a factor of 2 times the applied frequency ν_1. Thus penetration of the applied field should be substantial and analysis of the numerical space-charge potentials from the PIC calculations show this to be the case.

The PIC calculations in fact indicate that the mechanism of plasma loss involves the interaction of the applied field and the induced space-charge field at the edge of the plasma. That interaction is qualitatively described below in terms of a variant of the UCC model introduced in the previous part of this section. A more detailed description in terms of the PIC ion distributions will follow.

Consider a UCC model for two superimposed uniform cylindrical ion distributions of opposite sign. Assume that the ion dynamics is such that the ion distributions remain uniform. (This is rigorously true only for one-ion distribution.) Each ion distribution is then characterized by only its radius, $R_+(t)$ or $R_-(t)$, which obeys an equation similar to Eq. (20) with the inclusion of the space-charge force from the oppositely charged distribution. For example, from Eqs. (16) and (20), the equation for $R_+(t)$ is

$$\ddot{R}_+(t) + \omega_{f+}^2 R_+(t) = \begin{cases} \dfrac{2e^2(I/\dot{z}_0)}{m^+}\left(\dfrac{1}{R_+(t)} - \dfrac{R_+(t)}{R^2_-(t)}\right), & R_+(t) < R_-(t) \\ 0, & R_+(t) > R_-(t) \end{cases}, \tag{24}$$

where the " + " subscript denotes quantities whose values differ for the two distributions. Since $\omega_{f+} \neq \omega_{f-}$, the applied field will cause the initially identical radii of the two distributions to become different. Then, from Eq. (24), the space-charge force will act only to increase the smaller radius. If the applied field were to be turned off after inducing a small difference in the two radii, Eq. (24) would predict that space-charge forces would increase the sum of the two radii while inducing in their difference oscillations at the plasma frequency [Eq. (12)] with the reduced mass μ changed to the mass of the moving ion, m_+ or m_-. With the applied field on, the motion is a complicated one with space-charge forces acting to expand the ion distributions on a scale related to the plasma frequency.

This description in terms of the UCC model leaves out two important effects. First, the ion distributions do not remain uniform. In the larger distribution, only ions on the very edge of the distribution feel negligible space-charge forces. Ions near the edge of the oppositely charged smaller distribution feel a contractive space-charge force. This results in a tearing of the larger distribution at its edges. Second, at high-plasma density, the applied field is poorly approximated by the radial harmonic field for fundamental frequency oscillations. If the plasma frequency is comparable to ν_1 and thus much larger than ν_f, then the space-charge forces can respond to the actual, rather than effective, quadrupole field. That field is periodically contractive and expansive in one direction in the x,y plane while being the opposite in the orthogonal direction. If space-charge forces generally act to expand the edge of each distribution in the plasma, then, in a given direction, the additional acceleration of ions at the edges of the distributions is periodically reinforced by the applied field, which increases linearly from the axis. At sufficient plasma density, succeeding edges of each distribution will be periodically swept out of the QMF

until the plasma density and plasma frequency is sufficiently reduced. At low enough plasma frequency, the space-charge-induced expansion of the edges of each distribution is too slow and weak to be periodically reinforced by the applied field.

This simplistic analysis is in large measure borne out by a detailed study of the temporal behavior of the ion distributions in the PIC calculations. That behavior is presented in Figs. 6 and 7, where, for Cs^+ and UF_6^-, respectively, one quadrant of the calculated spatial distribution of the ions is displayed for four different times for $V_1 = 14.8$ kV and for an input current of 403 μA. The full spatial distribution of the ions at any one time can be generated by reflection symmetry from the displayed quadrant. The tick marks along the border measure off 2-cm intervals in either the x or y direction and the dark heavy lines denote the x and y axes. Note that the x and y scales are not the same so that the actual square region is represented in the figure as a rectangular region.

The four times displayed in Figs. 6 and 7 are $0.25/\nu_1$, $0.75/\nu_1$, $1.25/\nu_1$, and $1.75/\nu_1$, where zero time marks the creation of the plasma in the QMF. Since the initial phase of the applied field was zero for the calculations, these are the first four times at which the applied field is zero. Thus the direction of the applied field inverts at these times, and the changes in the charge distribution indicate the cumulative effect of the applied field over the time since its previous change of direction. The charge distribution shown is shaded when it extended beyond, and lined when it fell within, the charge distribution in the absence of space-charge effects. The outline of the charge distribution of both ions (beaded outline is for UF_6^-) in the absence of space-charge forces is also indicated in each section of the two figures.

Close examination of Figs. 6 and 7 reveals the following sequence of events. The initial contraction of each distribution by the applied field (which occurs in orthogonal directions for the two ions) is resisted by space-charge forces, which tend to stretch the distribution out to cover the distribution of the opposite ion. The initial expansion of each distribution by the applied field is enhanced by the space-charge forces. This can be seen for Cs^+ in the $0.25/\nu_1$ quadrant in Fig. 6, where there are shaded regions in both the vertical and horizontal directions. UF_6^-, with a heavier mass, responds more slowly, and so the effect is not obvious in Fig. 7 until a later quadrant.

After the applied field changes directions, it acts to reverse the motion it induced previously. The space-charge forces that resisted contraction previously continue, but now work in concert with the applied field to produce considerable expansion. The space-charge forces that previously abetted expansion continue, but now resist the applied field so as to reduce contraction. These effects are clearly seen for both UF_6^- and Cs^+ in the $0.75/\nu_1$ quadrants of Figs. 6 and 7.

After the applied field changes direction a second time at $0.75/\nu_1$, it again tries to reverse the previous motion.

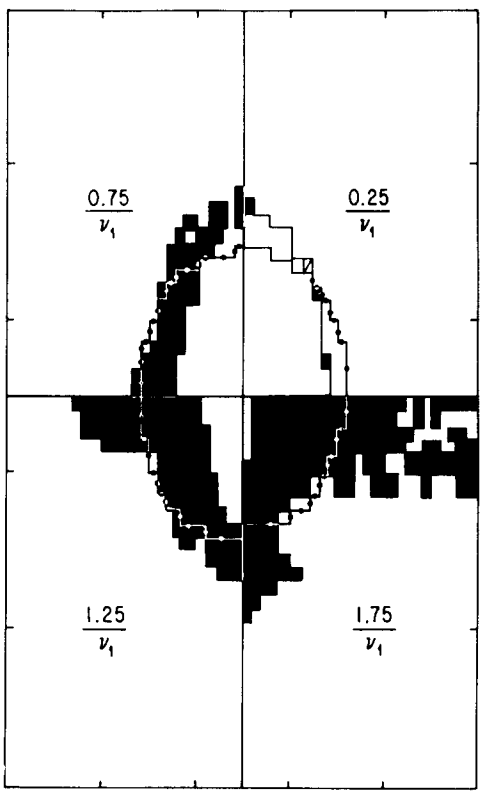

FIG. 6. Outline of one quadrant of the calculated Cs^+ distribution, for $V_1 = 14.8$ kV, $\nu_1 = 0.8$ MHz, and an input flux of 403 μA, at the four different times listed. The shaded region indicates extension beyond, and the lined region indicates contraction within, the same Cs^+ distribution in the limit of no space-charge forces. The outline of the UF_6^- distribution in the limit of no space-charge forces is indicated by the dot-solid curve. R_0 is 2.0 cm. Each tick mark in the horizontal or vertical direction denotes 2.0 cm.

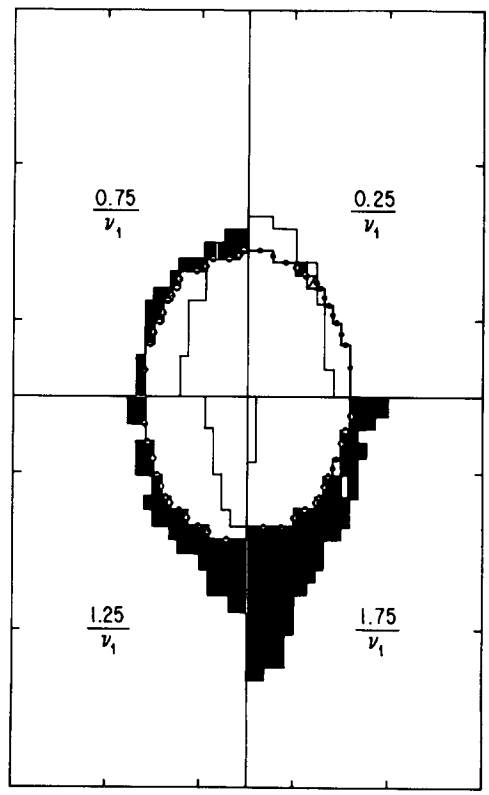

FIG. 7. As in Fig. 6 for UF_6^-. The Cs^+ and UF_6^- distributions in the limit of no space-charge forces are denoted by the solid curve and the dot-solid curve, respectively.

However, the unusually rapid expansion produced by the preceding concerted action of applied and space-charge fields is difficult to stem; and when the distribution expands beyond that of the opposite ion, the space-charge field does not switch signs at the edge but continues to push the edge ions farther out, in opposition to the applied field. The previous contraction is reversed with space-charge and applied fields working in concert. These effects, especially the largely unreversed expansion, are seen for both UF_6^- and Cs^+ in the $1.25/\nu_1$ quadrants of Figs. 6 and 7, respectively.

After the applied field changes directions a third time at $1.25/\nu_1$, the largely unchecked expansion that was not properly reversed in the preceding time is now in phase with the applied field. Furthermore, the distribution is considerably extended in that direction, and the strength of the applied field grows with distance from the axis. The space-charge force still works to expand the edge, but its effect declines as the charge density in the extending lobe declines. However, nearer to the edge of the distribution of the opposite ions, the space-charge forces act to contract the lobe. As a result of opposite space-charge forces on the edge of the lobe and on the edge of the other distribution, the lobe fragments. In the opposite direction, the ion motion produced by the concerted action of the preceding applied and space-charge fields is difficult to check. Furthermore, space-charge forces act to expand the distribution in an effort to catch up with the grossly extended lobe of the opposite ion's distribution.

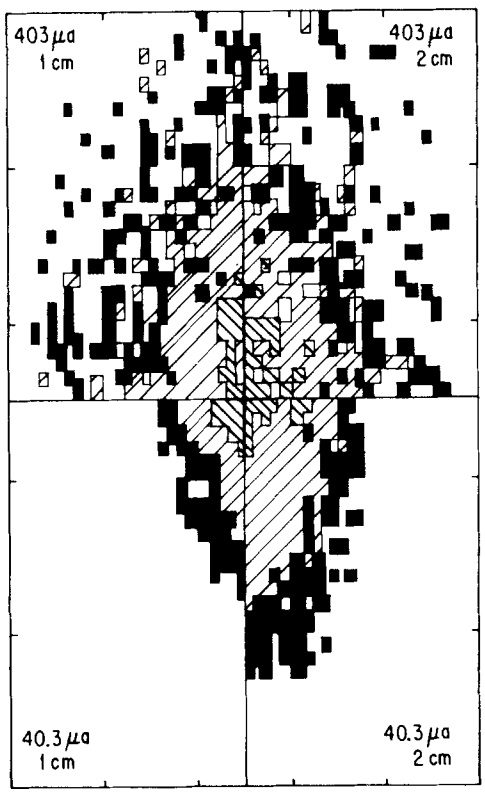

FIG. 8. Calculated UF_6^- distribution for $V_1 = 14.8$ kV and $\nu_1 = 0.8$ MHz at 5.25% of the transit time as a function of input current and initial radius. Each tick mark in the horizontal and vertical directions denotes 2.0 cm. The shaded and lined, lined, and dark areas denote plasma densities within 50, within 10, and below 10% of the maximum calculated density, respectively.

These effects are clearly seen for both UF_6^- and Cs^+ in the $1.75/\nu_1$ quadrants of Figs. 6 and 7.

The final result of these effects is graphically illustrated in Fig. 8 in which one quadrant of the calculated UF_6^- distribution is illustrated at a time of $24/\nu_1$ for both 403 and 40.3 μA input current and for an initial plasma radius of 1.0 and 2.0 cm. The markings on the distributions indicate ion densities within 50% (shaded and lined), 10% (lined), or below 10% (dark) of the maximum density. At the higher input current, the distributions show a natural evolution from Fig. 7, with a fraying of the distribution in both directions, a loss of memory of the initial radius, and a 25% loss of the initial number of ions. In addition, the bulk of the plasma seems to have expanded to about a 3-cm radius for the higher input current calculations. In contrast, for the lower input current where space-charge forces are reduced by an order of magnitude, the distributions show only minor evidence of fraying, a memory of the initial radius, and no loss of ions.

One final result implicit in Figs. 6 and 7 is that the lighter Cs^+ ion is lost preferentially. In Fig. 9, the loss of Cs^+ and of UF_6^- are traced as a function of the number of periods of the applied field. Clearly, the UF_6^- is playing an unsuccessful game of "catch-up" with the Cs^+. The lighter, more mobile Cs^+ leaves first, then its departure is retarded while UF_6^- is expelled. As the plasma approaches charge neutrality, other portions of the extended Cs^+ distributions tear away, get in phase with the applied field, and are swept away, prompting a further round of UF_6^- expulsion. This process is rapid at first when the plasma is dense. It slows down markedly as the plasma becomes less dense. Ultimately the plasma remains slightly negatively charged and the calculated Cs^+ confinement, as mentioned earlier, is slightly less than that of UF_6^-.

The results in Figs. 6–9 all were derived from a calculation at $V_1 = 14.8$ kV. The same effects are seen at reduced values of V_1, although they take longer to develop, because the applied field changes the initial distributions more slowly (i.e., the fundamental frequency is reduced). In a sense, the dynamics become more adiabatic, which might account for the fact that the calculated confinement curve for the highest input current peaks at lower values of V_1 (see Fig. 5). The

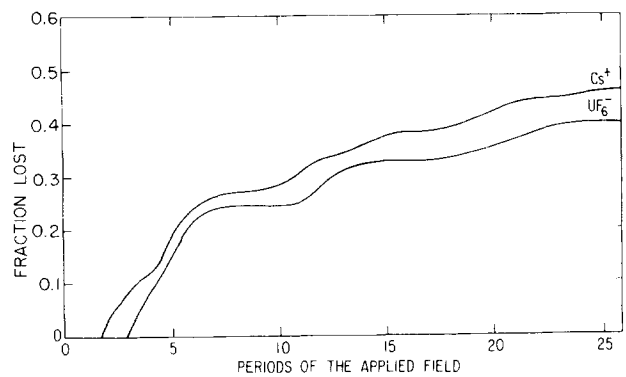

FIG. 9. Calculated fractions of UF_6^- and Cs^+ lost as a function of the elapsed number of cycles of the applied field. $I = 403$ μA, $R_0 = 2.0$ cm, $V_1 = 14.8$ kV, and $\nu_1 = 0.8$ MHz.

same effects are also seen at reduced values of the input current. However, at 40.3 μA the plasma is not dense enough to drive Cs^+ atoms out, and the plasma merely expands. Finally, these effects are also seen at $\nu_1 = 0.4$ MHz. They cause the loss of confinement at values of V_1 below the value where Cs^+ leaves altogether (see Fig. 4).

E. Limits on the transmitted current

From the calculations for both $\nu_1 = 0.4$ and 0.8 MHz, it appears that space-charge forces operate in such a way that, as the input current increases, the fraction lost within the QMF will increase. This is shown in Fig. 10. The figure plots calculated output current versus input current at $V_1 = 14.8$ kV for both $\nu_1 = 0.4$ and 0.8 MHz. The calculations were followed for only 44 and 21% of the transit time for $\nu_1 = 0.4$ and 0.8 MHz, respectively, but the loss of flux for the rest of the transit time is estimated to be less than 10%. The calculations were of the same quality as those which produced the confinement curves in Figs. 4 and 5. The results for $\nu_1 = 0.8$ MHz indicate that the maximum current that can be passed through the QMF is about 175 μA, independent of the input current. In fact, the maximum current ever observed experimentally at this value of V_1 for $\nu_1 = 0.8$ MHz was about 200 μA, although no systematic plot of output versus input current was performed. The same can be said for $\nu_1 = 0.4$ MHz, where the largest current observed experimentally was slightly less than 100 μA. The calculated limit from Fig. 10 is about 65 μA.

In the case of $\nu_1 = 0.4$ MHz, where the plasma is rapidly destroyed in the QMF, the calculated output limit is that imposed by space-charge blowup of a distribution of identically charged ions. For the case of $\nu_1 = 0.8$ MHz (or $\nu_1 = 0.4$ MHz at low values of V_1), where the plasma is retained, the physical basis underlying the calculated output limit is the general space-charge induced expansion of the edges of the ion distributions in the plasma. That expansion is at a frequency related to the plasma frequency. When that frequency is comparable to or exceeds the applied frequency, the expansion couples with the applied field to strip away the outer layers of the plasma. When the plasma density is reduced below a critical level, the plasma is too sluggish to effectively interact with the applied field.

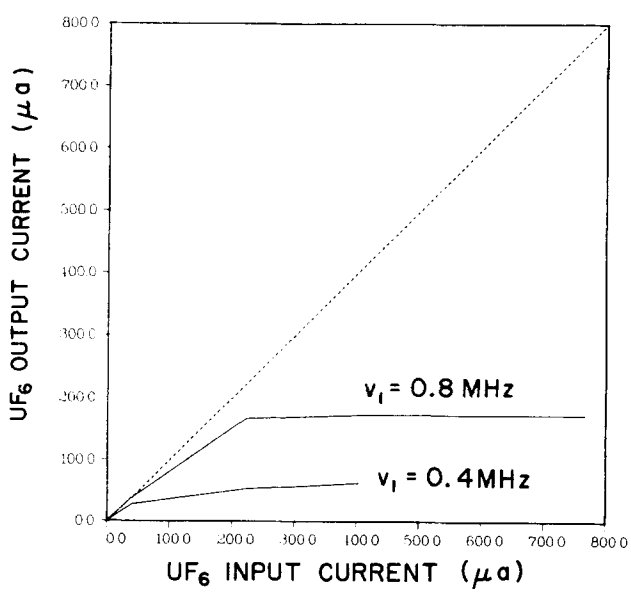

FIG. 10. Calculated output current as a function of the input current for $V_1 = 14.8$ kV, $\nu_1 = 0.8$ or 0.4 MHz, and $R_0 = 2.0$ cm. The diagonal dotted line indicates the current if confinement were perfect.

From Fig. 10, the use of a plasma to suppress space-charge blowup appears to increase transmitted current by only a factor of 3. This is in fact an underestimation because the limiting current for a single distribution of identically charged ions is much less for the case of $\nu_1 = 0.8$ MHz than it is for the case of $\nu_1 = 0.4$ MHz in Fig. 10. Since ν_f is approximately halved when ν_1 is doubled [see Eqs. (3), (5), and (6)], the applied field is, in effect, weaker. From the UCC model for one-ion distribution, this weaker effective field results in more than a factor of 4 reduction in transmitted current for $\nu_1 = 0.8$ MHz from that for $\nu_1 = 0.4$ MHz. Consequently, the use of a plasma increases throughput by at least an order of magnitude for $\nu_1 = 0.8$ MHz.

Both approximations in the PIC model and compromises in the numerical accuracy of the PIC calculations are such that the calculated limits in Fig. 10 cannot be taken as quantitative. However, the PIC results do support the qualitative conclusion that UF_6^- transmitted currents from the UF_6^--Cs^+ plasma will not exceed a milliampere, and the use of a plasma will not have improved transmission by more than two orders of magnitude. Experimentally, currents in excess of a milliampere were never obtained, although a definite limiting throughput was never observed.

IV. FRINGE-FIELD EFFECTS ON CONFINEMENT

The experimental record indicates a strong sensitivity of the confinement curves at high plasma densities to the manner of plasma formation. Specifically, plasma formation outside the QMF (crossed-beam plasma injection, see Fig. 5 of Paper I) results in a degradation of confinement curves at the higher densities and at higher values of V_1. However, degradation is much less severe for plasma formation within the QMF (merged-beam injection, see Fig. 7 of Paper I). Since the crossed-beam method forms the plasma entirely outside the QMF, the interaction of fringe fields (not included in any of the calculations so far) with space-charge forces may be responsible for the observations. While the necessary three-dimensional PIC calculations appropriate for a direct simulation are too expensive to perform, there is indirect theoretical support for this explanation, and this will now be examined. The measured confinement curves are also sensitive to the manner of extraction and detection of the ions exiting the QMF (see Fig. 8 of Paper I). Presumably, exit fringe fields interacting with space-charge forces are at work here, but the fields are too complicated to draw any significant dynamical inferences in the absence of full three-dimensional calculations.

Discussion of fringe-field effects must begin with the fringe-field potential. For simplicity, a simple model of the potential was used, in which the four hyperbolic poles are replaced by four lines of equally dense charge, of the appro-

priate sign, running the length L of the mass filter. If z measures the displacement from the QMF entrance along its axis ($z>0$ for inside the QMF), if $\pm r_0$ is the off-axis displacement of the lines of charge in the xz or yz plane, and if the line-charge density is adjusted to reproduce the perfect quadrupole field deep within the QMF, then the potential $V(x,y,z)$ generated by the lines of charge for small off-axis displacements relative to r_0 is

$$V=[U-V_1\cos(2\pi\nu_1 t)]\frac{x^2-y^2}{2r_0^2}\frac{F(z)}{F(L/2)}, \tag{25}$$

where

$$F(z)\equiv\int_0^L [r_0^2+(l-z)^2]^{-5/2}dl. \tag{26}$$

The entire z dependence of the potential is contained in $F(z)$, which has a straightforward, though involved, analytic expression that will not be presented here. Equation (25) does not apply for most of the experiments, since they were performed with a grounded metal plate inserted parallel to, and 2.5-cm upstream from, the QMF entrance plane. (The plate contained a hole for passage of the plasma.) By imaging, the fringe potential of Eq. (25) can be modified to give a zero potential plane at $z=-d$, and thus mimic the effect of the plane. The result is

$$V=[U-V_1\cos(2\pi\nu_1 t)]\frac{x^2-y^2}{2r_0^2}\times\left[\frac{F(z)-F(2d+L+z)}{F(L/2)}\right]. \tag{27}$$

From $z=-d$ to 0, the bracketed factor varies approximately linearly from 0 to about 0.5. By $z>r_0$, the bracketed factor is nearly unity. Both potentials [Eqs. (25) and (27)] were derived under the condition that x^2+y^2 is much less than $r_0^2+z^2$; for larger displacements, they underestimate the magnitude of the actual potential.

To determine the effect of fringe fields at low densities, trajectories were followed with the potential given by Eq. (27). As in the PIC calculations of the preceding section, the initial axial velocity was 1.75×10^5 cm/sec and the initial maximum off-axis velocity was 0.316×10^5 cm/sec. The initial plasma radius, R_0, was varied. Since the crossed-beam plasma formation was used for only $\nu_1=0.8$ MHz, this frequency was employed in all calculations. The initial phase of the field was varied and the results were phase averaged. Ions were considered lost if their trajectories struck the electrodes or the grounded plate (after reflection).

The resulting calculated percentages of UF_6^- ions lost in the fringe field as a function of V_1 and R_0 are listed in Table III. The calculated ion losses increase with increasing V_1 or R_0 because the ions, in either case, are exposed to stronger fringe fields. For $R_0<2$ cm, ion losses for all values of V_1 in the table are relatively minor. This is true despite the fact that the maximum change in the potential from the grounded plate to deep within the QMF is typically several orders of magnitude larger than the initial axial energy of the ions. The rapid oscillations of the field (tens of cycles during fringe-field penetration) sufficiently reduce the average or effective potential gradient to allow nearly complete transmission for $R_0<2$ cm. Such values of R_0 also characterize the initial experimental plasma distributions. The calculated minor losses in the fringe field for these values of R_0 are consistent with the experimental observation of little degradation of the confinement curves at high V_1 for low density plasmas with the crossed-beam injection method (see Fig. 10 of Paper I).

For $R_0\geqslant2$ cm, the results in Table III indicate severe ion loss in the fringe field. If space-charge forces at high plasma densities could cause an initial plasma distribution formed outside the QMF to expand beyond 2 or 3 cm in the time it takes to traverse the entrance fringe field, then loss by reflection could be severe. Such an expansion can be deduced in the following way from PIC calculations performed for a pure quadrupole field. In Fig. 11, the maximum radial displacement of UF_6^- is displayed as a function of periods of the applied field for plasmas with input currents of 40.3 and 403 μA. For each input current the values for $V_1=1$ and 14.8 kV are marked, and the space between them is lined in. Although the results displayed in the figure have been calculated for a pure quadrupole field, the strength of the entrance fringe field will vary from a low value up to the final value of 14.8 kV in traversing the fringe field of a QMF set at $V_1=14.8$ kV, and in a qualitative way the spatial extent of the UF_6^- will fall within the lined region. The smaller the final value of V_1, the more the UF_6^- spatial extent will fall in the lower portion of the lined region. The 10 cycles of field indicated in the figure can be compared to the approximately 12 cycles that occur during unimpeded passage from the grounded plate to the entrance plane of the QMF. The figure shows that at input currents measured in tens of microamps, the UF_6^- will not expand very much beyond its initial radius of 1 cm at low values of V_1. At high values of V_1, its initial size may double or triple. However, at input currents measured in hundreds of microamps, even at low values of V_1 large expansions of the UF_6^- occur, and the expansions grow more severe as V_1 increases. Similar plots for Cs^+ would display even greater expansions. Since, from Table III, axial reflection of ions with radial displacements beyond 2 cm is an important effect, it is not surprising that degradation of the confinement curve due to entrance effects should become significant for fluxes of greater than 10 μA.

In the next two sections, the effect of a combined quadrupole-dipole field on plasma behavior will be investigated. Experimentally, the additional field does not produce further qualitative differences between confinement curves for the crossed- and the merged-beam injection methods. This is evidence that the additional dipole fringe field does

TABLE III. Percentage of UF_6^- ions lost in the fringe field of Eq. (27) as a function of V_1 (kV) and R_0 (cm).

R_0 (cm)\ V_1 (kV)	5	10	15
1	0.0	0.0	13.3
2	0.0	46.7	77.0
3	24.2	75.3	93.9
4	47.8	82.8	96.1

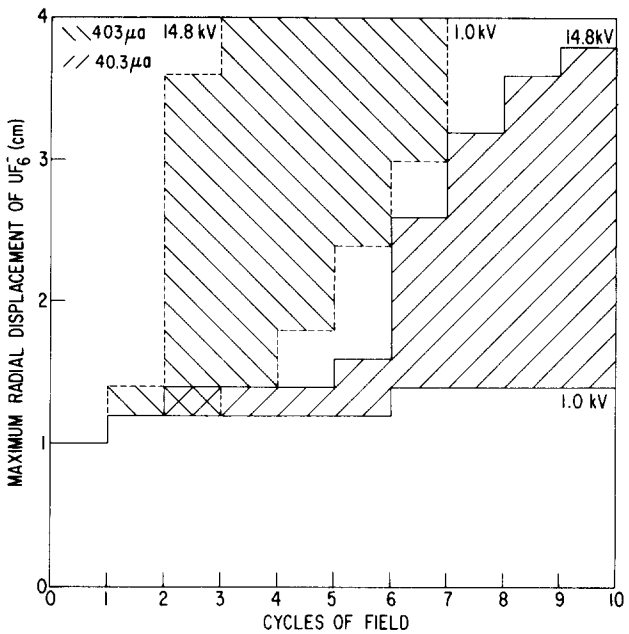

FIG. 11. Calculated maxinum radial displacement of UF_6^- as a function of the elapsed cycles of the field for $\nu_1 = 0.8$ MHz, $V_1 = 14.8$ or 1.0 kV, and $I = 40.3$ or 403 μA. R_0 is 1.0 cm. The enclosed region indicates where displacements for V_1 between 1.0 and 14.8 kV are expected to fall.

not substantially alter ion transmission. Trajectory calculations similar to those presented in Table III confirm this interpretation.

V. LOW-DENSITY ION EJECTION IN COMBINED QUADRUPOLE-DIPOLE FIELDS

A. Brief review

In this section, as in Sec. II, the behavior of ion distributions in the absence of space-charge force is considered. The results therefore apply to only low density plasmas. In Sec. II, it was shown that a perfect quadrupole field induces off-axis oscillatory ion motion whose spectrum of frequencies is dependent upon the ion mass m and the applied quadrupole frequency ν_1 and amplitude V_1. In this section, the theory is extended to include an additional, nonconfining oscillatory dipole field of frequency ν_2 and amplitude V_2, and to thereby describe the resonance behavior of ions of a specific mass with an applied quadrupole-dipole field. This theory shows that at resonance a weak dipole field can drive ions of a specific mass into ever-expanding orbits such that the ions eventually strike the poles of the mass filter, resulting in loss of transmission. Thus the system operates to confine all ions (within the stability diagram) except the specific one that is being ejected by the applied weak dipole field. In this ion-ejection mode, the QMF acts as a mass separator, but uses no d.c. fields. In the conventional use of a QMF for mass separation, both d.c. and rf fields are used to place only the desired mass in the stability diagram (at its tip; see Fig. 1). However, d.c. fields cannot penetrate dense plasmas and so will not be used here.

The well-developed theory for ion behavior in a combined quadrupole-dipole field is reviewed in Dawson and Whetten.[2] Its pertinent features will be briefly examined here followed by application of the theory to the calculation of Cs^+-UF_6^- behavior in the QMF. These results can be directly compared to measurements discussed in Sec. VI of Paper I.

The dipole field in the QMF was generally applied from one pair of adjacent poles to the opposite pair of adjacent poles. Since the poles are hyperbolic in shape, the application of a sinusoidally varying potential in the dipole configuration produces a potential in the interior of the mass filter that is a complicated function of x and y. However, near the axis of the mass filter the actual shape of the poles exerts a minor influence on the potential, and the latter can be represented to a fair degree of accuracy as the sum of the two dipole potentials, each across opposite poles of distance $2r_0$ apart, but oriented 90° from one another. With this approximation, the electric potential of the QMF in the ion-ejection mode is:

$$V = [U - V_1 \cos(2\pi\nu_1 t)] \frac{x^2 - y^2}{2r_0^2} + V_2 \cos(2\pi\nu_2 t) \frac{x + y}{2r_0}. \quad (28)$$

The first term is the potential for a pure quadrupole field, Eq. (1); the second term is the additional dipole potential. The equation of motion in x for an ion of charge $\pm e$ and mass m is

$$\frac{d^2x}{d\xi^2} \pm (a_x - 2q_x \cos 2\xi)x \pm \eta \cos\left(\frac{\nu_2}{\nu_1} 2\xi\right) = 0, \quad (29)$$

where

$$\eta = \frac{2eV_2}{m(2\pi\nu_1)^2 r_0}, \quad (30)$$

and where a_x and q_x are defined in Eq. (3). A similar equation exists for motion in y with the signs of a_x and q_x reversed.

Equation (29) contains an inhomogeneous term that distinguishes it from Eq. (2) for ion motion in the absence of a dipole field. A general form for the solution to Eq. (29) is

$$x(\xi) = x_h(\xi) + x_p(\xi), \quad (31)$$

where x_h is the solution to the homogeneous equation obeying all the initial conditions, and x_p is the particular solution to the inhomogeneous equation, with initial conditions

$$x_p(t_0) = \dot{x}_p(t_0) = 0. \quad (32)$$

x_h is exactly the solution to ion motion in a quadrupole field alone, i.e., Eq. (4), which provided all the results discussed in Sec. II. The effect of the dipole field is in x_p which has the same initial conditions, i.e., Eq. (32), independent of the initial conditions on the trajectory $x(\xi)$. In other words, x_p is the same for all ions no matter where they are originally located in the initial ion distribution.

x_p has a complicated analytical solution available in Dawson and Whetten.[2] The essential features of this solution can be more simply illustrated by the fundamental-mode version of Eq. (29), in which the quadrupole field is replaced by the harmonic field that induces the same fundamental frequency as the original field. Equation (29) for x_p then reduces to

$$\ddot{x}_p + \omega_f^2 x_p - (\pi\nu_1)^2\eta\cos(2\pi\nu_2 t) = 0, \tag{33}$$

which, for the boundary conditions of Eq. (32), has the solution

$$x_p = \frac{\nu_1^2\eta}{2(\nu_2^2 - \nu_f^2)}\sin\left(2\pi\frac{\nu_2+\nu_f}{2}t\right)\sin\left(2\pi\frac{\nu_2-\nu_f}{2}t\right) \tag{34}$$

$$\xrightarrow[\nu_f\to\nu_2]{} \frac{\nu_1^2\eta}{2(\nu_2+\nu_f)}\pi t\sin(2\pi\nu_2 t).$$

For the full quadrupole field, the solution for x_p is more complicated but similar in form to that here, with one exception. Since the quadrupole field induces a spectrum of frequencies [see Eq. (4)], any one of them can be brought into resonance with the dipole field. The fundamental frequency in Eq. (33) is that frequency out of the spectrum which has the largest amplitude. If any other frequency is brought into resonance, the solution for x_p is similar to Eq. (34), but reduced by the ratio of the frequency's amplitude to the amplitude of the fundamental frequency. Under conditions of the experiments, that ratio is typically one-tenth or less.

From Eq. (34), at resonance, x_p contains an oscillatory term whose amplitude grows linearly with time in the QMF. Since ν_f is a function of β and β is a function of V_1, variation of V_1 for a fixed ν_2 brings ν_f into resonance with ν_2. Thus two ions whose β values differ because of their masses can be separated by placing one mass exactly at resonance. The dipole field will introduce into the ion trajectories an oscillatory perturbation, whose amplitude will increase with time in a linear fashion for the resonant mass, but whose amplitude will vary only sinusoidally for the off-resonance mass. By adjusting V_2 the strength of the perturbation, as measured by η, can be selected so as to transmit the off-resonant mass through the QMF while ejecting the resonant mass. The auxiliary dipole field can be made to resonate with any one of different frequencies present in the ion motion in a pure quadrupole field. However, the price of selecting any frequency other than the fundamental frequency is the necessity of using large values of V_2 to overcome the reduced amplitude of that frequency. Regardless of the frequency used, the objective is to obtain the sharpest possible resonance for a given mass so as to maximize the resolving power of the mass filter.

Experimentally, the major method of characterizing plasma confinement and transmission in the QMF with a combined quadrupole-dipole field was the measurement of so-called resonance curves of transmitted ion flux as a function of V_1 for fixed ν_1, ν_2, and V_2. Clearly, when V_2 is zero, resonance curves become the confinement curves discussed in the previous three sections. The calculation of a resonance curve at low density consists of determining the fraction of transmitted trajectories according to Eq. (29) for a statistically significant number of ions in an appropriate initial distribution. However, as in the calculation of confinement curves, for a rather general set of initial conditions, the distribution of ions can be simply characterized in terms of a few parameters whose time dependence, i.e., trajectories, can be directly calculated. The resonance curve can then be calculated from the time dependence of the distribution, thus avoiding the necessity and complication of calculating individual ion trajectories. The use of parameter trajectories will be described next, followed by the calculated resonance curves.

B. Parameter trajectories

In Sec. II B, it was shown that if the initial distribution of ions in the xy plane was circular or elliptic, if each ion's initial off-axis velocity was proportional to its displacement from the center of the distribution, and if all ions had a common axial velocity, then the distribution would always be ellipsoidal and therefore characterized by major and minor axes $a(t)$ and $b(t)$ and center $[x_c(t), y_c(t)]$. The equation for $a(t), b(t), x_c(t)$, and $y_c(t)$ is Eq. (2), with the appropriate initial value and time derivative for each parameter. From Eqs. (31) and (32), the dipole field causes the same additional displacement $x_p(t)$ and $y_p(t)$ to every ion regardless of its position in the initial distribution. Hence the dipole field moves the ion distribution as a whole in the xy plane, or in other words, the dipole field affects only $x_c(t)$ and $y_c(t)$. Therefore, in a combined dipole-quadrupole field with the same initial conditions as above, the distribution is still characterized by axes $a(t)$ and $b(t)$ obeying Eq. (2) and by a center $[x_c(t), y_c(t)]$ that now obeys Eq. (29). If the distribution is initially centered and directed along the axis, then the initial conditions on $x_c(t)$ are exactly Eq. (32) and $x_c(t)$ is exactly equal to $x_p(t)$. The entire ellipse, which would have remained centered on the QMF axis, is driven by the dipole field into oscillations about the axis, with amplitudes controlled by resonance effects.

C. Calculated resonance curves

The remaining discussion of the low-density theory will be directed to the calculation of resonance curves. As in the confinement calculations, the ion distribution parameters $a(t), b(t), x_c(t)$, and $y_c(t)$ are directly calculated, and the overlap of the resulting distribution with the QMF poles during the transit time determines the transmitted fraction.

For a mass filter of the experimental dimensions, initial distributions of Cs^+ and UF_6^- in the form of a circle of radius 1.0 cm about the quadrupole axis, a maximum initial off-axis ion velocity of 0.1 km/sec, and a constant on-axis ion velocity of 1.5 km/sec, trajectory calculations predict the resolution curves in Fig. 12(a) for $\nu_1 = 0.8$ MHz and $\nu_2 = 0.0363$ MHz, and in Fig. 12(b) for $\nu_1 = 0.4$ MHz and $\nu_2 = 0.0727$ MHz. In both cases two resonance curves are shown, one corresponding to collection of UF_6^- and the other of Cs^+. In each case V_2 was selected to be just large enough to drive the UF_6^- resonance to zero transmission ($V_2 = 20$–27 V). Off-resonance, the curves are essentially unchanged from the corresponding confinement curves in Fig. 2 (except for the dipole field, the calculations presented in Figs. 2 and 12 are identical). Figure 12(b) also shows the ejection of Cs^+ when V_1 is greater than ~ 7 kV, which results from this species being no longer within the stability diagram [see Fig. 2(b)].

Figure 12 shows little change in the location of the resonance if ν_1 is changed from 0.8 to 0.4 MHz. This is as expect-

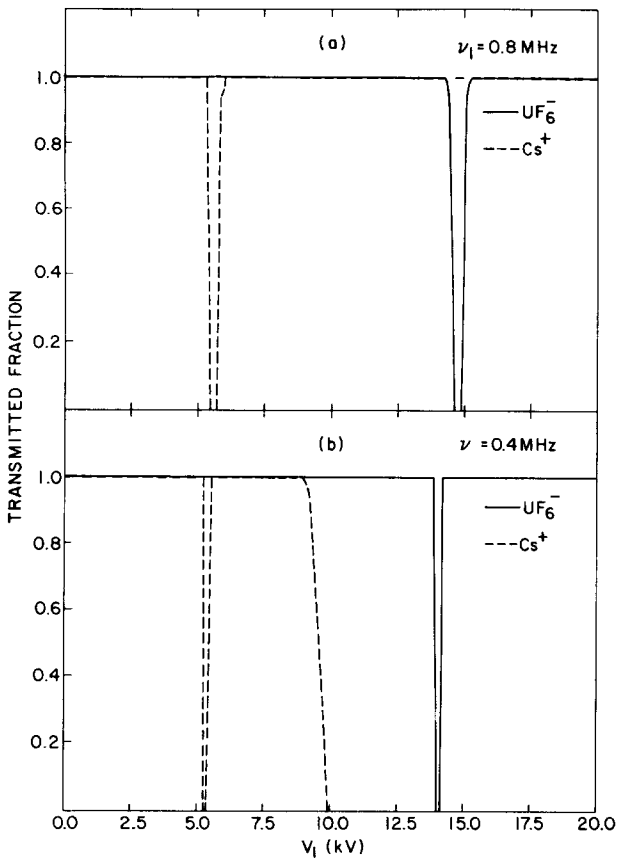

FIG. 12. (a) Resonance curves for UF_6^- (solid curve) and Cs^+ (dashed curve) calculated from low-density theory for $\nu_1 = 0.8$ MHz, $\nu_2 = 0.0363$ MHz, and $V_2 = 26$ V; (b) as in (a) for $\nu_1 = 0.4$ MHz, $\nu_2 = 0.0727$ MHz, and $V_2 = 27$ V.

ed for if V_r is the value of V_1 at resonance, i.e., $\nu_f = \nu_2$, then from Eqs. (3), (5), and (6), V_r obeys the relation

$$V_r \propto m\nu_1^2\left(\frac{\nu_2}{\nu_1}\right)\left[1 - \frac{3}{2}\left(\frac{\nu_2}{\nu_1}\right)^2\right]. \tag{35}$$

If ν_1 is halved and ν_2 is doubled, Eq. (35) predicts V_r will change little if $\nu_2 \ll \nu_1$. Figure 12 shows a smaller value of V_r for Cs^+ than for UF_6^-. Equation (35) predicts this also. Finally, Fig. 12 shows a sharper resonance for the lower value of ν_1. From Eq. (34), the approach to resonance is governed by the difference $(\nu_2 - \nu_f)$. Since ν_f is approximately proportional to V_1 but inversely proportional to ν_1, a fixed increment in V_1 will make a larger change in ν_f the smaller is ν_1. Hence sharper resonances are expected for smaller values of ν_1.

D. Comparison to experimental measurements

The calculated resonance curves reproduce many of the low-density experimental measurements in Paper I, as found in Figs. 14, 17, 23, and 24 (for currents below 1.5 μA) of that paper. The experimental shape of the resonance and associated magnitude of V_2 are qualitatively similar to the calculated results in Fig. 12. The location of V_r of the experimental resonance is only 0.2–0.6 kV higher than the theoretical location for $\nu_1 = 0.8$ MHz and 0.1–0.3 kV higher than the theoretical location for $\nu_1 = 0.4$ MHz. These differences are probably within the errors to which V_1 is known experimentally (owing to calibration difficulties). The calculated decreased resonance width with decreased size of ν_1 appears to be confirmed by Figs. 17 and 24 of Paper I. However, the measured resonance width is affected by the precise manner of extraction and detection (as seen in Fig. 17), and the results in the two figures did involve different extraction and detection fields. Nevertheless, it appears that all the theoretical features of the resonance are qualitatively confirmed by the experiment at the lowest densities.

Even at the lowest experimental densities, however, there are additional features in the experimental results that are not expected from the calculations. The most important of these is an additional resonance in each resolution curve occurring at the location of the resonance for the oppositely charged ion. For example, at an output current of 0.2 μA the resonance curve for Cs^+ in Fig. 14 of Paper I shows a loss of Cs^+ confinement at that value of V_1 where UF_6^- confinement undergoes a resonance. This is clearly a space-charge effect neglected entirely in the low-density calculations. The same figure also shows another unexpected resonance at low values of V_1 below the Cs^+ resonance location. This is probably due to space-charge effects, as will be discussed.

At higher densities, the experimental resonance curves become noticeably different from the calculated results of Fig. 12. For $\nu_1 = 0.4$ MHz, as seen in Fig. 25 of Paper I, the UF_6^- resonance requires much higher values of V_2 to drive the bottom of the resonance to zero transmission. At the higher values of V_2 the resonance is broad and more rounded at the bottom. A small satellite resonance on the low-V_1 side of the major resonance also develops. However, the location of the major resonance remains the same, within experimental error, to that calculated by the low-density theory. At low values of V_1 below the location of the Cs^+ resonance, loss of transmission occurs with increased V_2. This is not prominent in Fig. 25 of Paper I because of the difficulties in extraction and detection at low V_1 (see discussion in Sec. V of Paper I). Extraction fields that maximize the detection of low-V_1 confinement do result in resonance curves at high densities that have substantial plasma loss at high V_2 and low V_1.

For $\nu_1 = 0.8$ MHz, the high-density experimental resonance curves can be found in Figs. 20–22 of Paper I. They show, in contrast to Fig. 12, the same high values of V_2 and consequent loss of confinement at low V_1 found for $\nu_1 = 0.4$ MHz. In addition, they show additional resonances between the Cs^+ and UF_6^- resonance locations which grow with increasing V_2 into a broad deep loss of confinement on the low-V_1 side of the UF_6^- resonance. Finally, the location V_r of the experimental UF_6^- resonance varies with V_2 and ν_2 in ways completely unaccounted for by low-density theory. In general, increasing V_2 causes V_r to increase, often to more than 1 kV beyond the theoretical value. On the other hand, variations in ν_2 cause shifts in V_r one-tenth of that predicted by low-density theory, resulting in experimental values of V_r more than 2 kV below the theoretical value. Clearly, for $\nu_1 = 0.8$ MHz, the low-density theory offers a poor description of high-density resonance curves.

VI. HIGH-DENSITY ION EJECTION IN COMBINED QUADRUPOLE-DIPOLE FIELDS

The discrepancies between the results of low-density theory and the experimental measurements indicate that many features of the resonance curves at high densities are qualitatively influenced by space-charge effects. To study these effects, the PIC trajectory model of Sec. III was extended to include dipole fields. In the first two parts of this section, the relevant plasma parameters and the incorporation of a dipole field into the PIC model will be briefly discussed. In the two remaining parts of this section, the calculated resonance curves and the mechanisms for plasma loss in a combined quadrupole-dipole field will be discussed, first for $\nu_1 = 0.4$ MHz and then for $\nu_1 = 0.8$ MHz. Both the PIC results and simpler models of space-charge effects will be used in the discussion. In general, the results will be more difficult to interpret and the relation to experiment will be less secure than in the case of confinement curves alone.

A. Plasma parameters

The parameters listed in Table I for confinement do not change on introduction of a dipole field. The dipole field frequency ν_2 to be used in the simulations is either 0.0363 MHz for $\nu_1 = 0.8$ MHz or 0.0727 MHz for $\nu_1 = 0.4$ MHz. Thus ν_2 is always smaller than ν_p listed in Table I, and is usually much smaller. This would imply that the dipole field will have difficulty penetrating the interior of the plasma. Furthermore, since at low density the dipole field induces a resonance by moving the ion distribution as a whole (see Sec. V B), penetration difficulties should have a significant effect on the resonance. As will be shown later, both these conclusions are confirmed by the PIC calculations.

B. Particle-in-cell model

The inclusion of a dipole field in the simulation introduces three practical difficulties in applying the PIC method to the calculation of resonance curves. First and most important, a simulation time almost as long as the experimental transit time is required before the final form of the resonance curve becomes apparent. For comparable confinement curves, simulation times only 10% of the transit time are all that are necessary. Longer simulation times increase the expense and, because of error accumulation, decrease the accuracy of the calculation. Second, the dipole field reduces the quadrupole symmetry, requiring the explicit calculation of the trajectories of more simulation particles (see Sec. III B). Although almost all the experiments were done with a dipole field applied across both pairs of poles, all the calculations will assume a dipole field applied across only one pair of poles in order to retain at least the symmetry of one plane of reflection. Last, two new variables, V_2 and the initial phase of the dipole field, must be scanned for a complete set of resonance curves for one combination of ν_1 and ν_2.

Because of these three complications, a very restricted set of calculations were performed at the higher input current of 403 μA. The initial phase of both the applied fields was set to zero in all calculations; no attempt was made to phase-average the results. As discussed in Appendix B, only the least expensive values of Δt, N_c, and N_p were selected, so only the grossest calculated features of the resonance curves can be assumed to be reliable. Errors of tens of microamperes in computed output current are possible. However, as will be seen shortly, the final curves seem in reasonable accord with experiment.

C. Results and analysis for $\nu_1 = 0.4$ MHz

1. Results

For $\nu_1 = 0.4$ MHz, the resonance portion of the UF_6^- resonance curve calculated with the PIC model is displayed in Fig. 13 along with an analogous calculation using the low-density theory of the previous section. For both calculations, the resonance curve has been normalized to unity at $V_1 = 17.8$ kV, the highest value of V_1 included in the PIC study. The values of R_0 and $v_\perp$ were 1 cm and 0.316×10^5 cm/sec, respectively. ν_2 and V_2 were 0.0727 MHz and 0.1 kV, respectively. The PIC simulation time was 87.5% of the experimental transit time. At high input current, the PIC confinement curve in the absence of a dipole field increases with V_1 (see Fig. 4), accounting for the drop in transmission on the low-V_1 side of the resonance in the PIC calculation in Fig. 13. In the low-density regime, confinement is perfect on either side of the resonance.

The calculated high-density resonance in Fig. 13 requires a much higher value of V_2 to drive the bottom of the resonance to zero transmission than that in the low-density theory. Furthermore, the width of the resonance at half-depth is larger for the higher density calculation. Both these

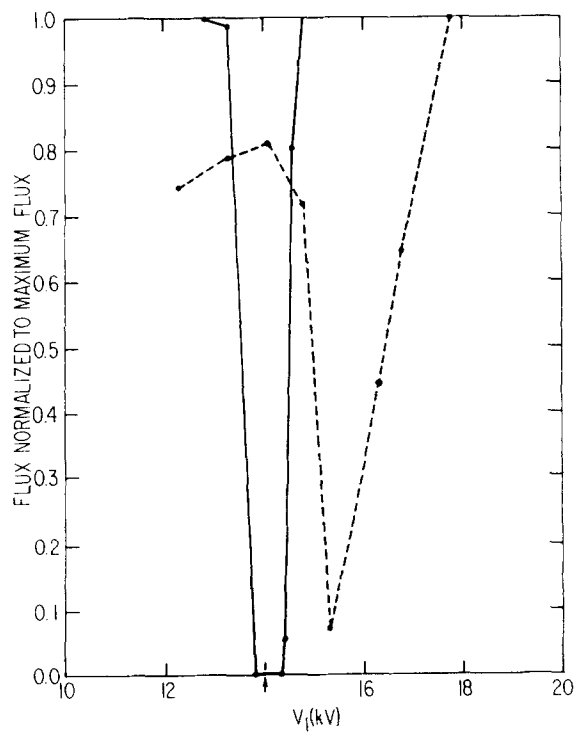

FIG. 13. High-V_1 portion of the resonance curve, normalized to unity at $V_1 = 17.8$ kV, as calculated with (dashed curve) and without (solid curve) space-charge coupling for $\nu_1 = 0.4$ MHz, $\nu_2 = 0.0727$ MHz, and $V_2 = 0.1$ kV. I is 403 μA.

features are in accord with experimental results. However, Fig. 13 also shows that the calculated resonance is shifted by ~ 1.5 kV upward from the resonance position determined from low-density theory. There is no evidence of such a shift in the experimental results (for $\nu_1 = 0.4$ MHz) and this constitutes a serious disagreement between theory and experiment.

2. Analysis

As in the confinement calculations for $\nu_1 = 0.4$ MHz, this disagreement between the PIC model and experiment is shared by a version of the analytic UCC model. To incorporate an additional dipole field into the UCC model, two further approximations are required. First, the loss of current in the quadrupole field is assumed to be so rapid that the dipole field effectively operates on the current $I_{\rm OUT}$ of Eq. (21). This is in accord with the much higher frequency and voltage of the quadrupole field. Second, the space-charge potential used is a simple limiting form of the exact potential required, namely, one for a uniform cylinder of charge displaced a distance x_c off-axis by the action of a dipole field in the x direction. To meet the boundary condition of zero value at the field radius r_0, the exact potential contains an infinite series of radial and trigometric functions in addition to terms analogous to those in the potential for a centered distribution, i.e., Eq. (16). In the limit of small displacements x_c, only the lead terms in the infinite series are required, and potential V_{sc} assumes the simple form

$$V_{sc}(r,\phi,z) = e(I_{\rm OUT}/\dot{z}_0)\left[\left(1-\frac{r^2}{R^2(t)}\right)+2\ln[r_0/R(t)] - \frac{2x_c(t)[r\cos\phi - x_c(t)]}{r_0^2}\right] \tag{36}$$

for r less than or equal to the distribution radius $R(t)$. Here r and ϕ are measured with respect to the center of the distribution, not the QMF axis.

V_{sc} is identical to that for $x_c = 0$ [Eq. (16)] except for the last term, which is dependent only on the x position (i.e., $r\cos\phi$) in the distribution. Furthermore, the dependence is linear, which makes the force in the x direction independent of position or the same for all ions in the distribution. These properties of V_{sc} can be used to show that the ion distribution in the applied and space-charge potential remains uniform and characterized only by a radius $R(t)$ and an x-displaced center $x_c(t)$. The equation for $R(t)$ is unchanged from that for a pure quadrupole field [Eq. (20)], while that for $x_c(t)$ is

$$\ddot{x}_c(t) + \left[\omega_f^2 - \frac{2e^2(I_{\rm OUT}/\dot{z}_0)}{mr_0^2}\right]x_c(t) = \frac{eV_2}{2mr_0^2}\cos 2\pi\nu_2 t. \tag{37}$$

The last term in V_{sc} is responsible for the ion-current-dependent term in the above equation. That term reduces the effective fundamental frequency of ion motion (i.e., the bracketed terms), thereby increasing the value of V_1 required to bring the effective frequency into resonance with the fixed dipole frequency. The resulting upward shift in resonance location can be calculated from Eq. (37) and the equations governing $I_{\rm OUT}$ (see Sec. III C). The results range from 1.3–3.5 kV shift for the same conditions listed in Table II for UCC confinement in a pure quadrupole field.

Even though Eqs. (36) and (37) are derived in the limit of small displacements (clearly not true at resonance), the UCC and PIC models produce similar kilovolt upward shifts in the resonance location that are not observed experimentally for $\nu_1 = 0.4$ MHz. As in confinement, the origin of the error is most likely approximations shared by both models. In the UCC model, the shift in resonance location is due to a term in V_{sc} that is required for the potential to meet spatial boundary conditions. In both the UCC and PIC models, these boundary conditions are highly simplified versions of the experimental boundary conditions. Thus approximations in the boundary conditions may account for the differences with experiment.

While the UCC and PIC models agree on the shift in resonance location, they disagree on the size of V_2 necessary to develop the resonance. The UCC model predicts no increase in V_2 from the low-density limit. This occurs because the approximations required to maintain a uniform distribution result in only one frequency characterizing the oscillation of the ion distribution as a whole [i.e., Eq. (37)]. In the PIC model, one of the effects of plasma loss and a rigorous inclusion of the applied field is a nonuniform distribution with a spectrum of density-dependent frequencies which share the oscillation amplitude exclusively possessed by one frequency in the UCC model. Since V_2 is inversely proportional to the amplitude of the oscillation brought into resonance, the size of V_2 needed to induce a deep resonance increases in the PIC model. Furthermore, a close-packed spectrum of frequencies produces a broader resonance for a given V_2 than expected otherwise, which is also seen in the PIC calculations. Both these features are in accord with experiment.

D. Results and analysis for $\nu_1 = 0.8$ MHz

1. Results

For $\nu_1 = 0.4$ MHz, the UF_6^- resonance curves calculated with the PIC model are displayed in Fig. 14 for

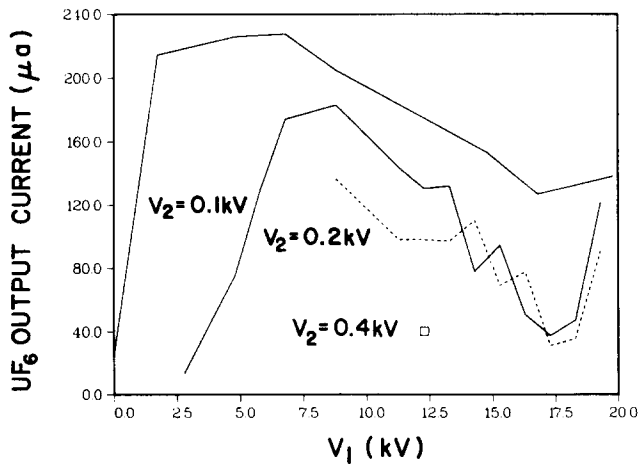

FIG. 14. Portions of the UF_6^- resonance curves as calculated with the PIC model for $\nu_1 = 0.8$ MHz, $\nu_2 = 0.0363$ MHz, $V_2 = 0.1$, 0.2, and 0.4 kV. I is 403 μA. The confinement curve from Fig. 5 is also traced.

$\nu_2 = 0.0363$ MHz and for $V_2 = 0.1$, 0.2, and 0.4 kV. In Fig. 15, the resonance portion of these curves are normalized to unity and compared to the analogous calculation for $V_2 = 0.1$ kV using the low-density theory. In all cases, R_0 and $v_\perp$ were identical to those used in the PIC calculation of confinement (Fig. 5), and the associated confinement curve is reproduced in Fig. 14. The simulation time for both resonance and confinement curves was 87.5% of the experimental transit time.

The calculated results in Fig. 14 qualitatively agree with the major features of the measured resonance curves in the high-density regime. These features include the relatively large values of V_2 necessary to obtain a substantial UF_6^- resonance, the broad loss of confinement at low values of V_1, the loss of confinement at intermediate values of V_1 with increasing V_2, and finally the shift of the UF_6^- resonance to larger values of V_1 with increasing V_2. None of these features are properly accounted for by low-density theory (see Sec. VI C 2). However, the PIC resonance curves show a much more gradual variation with V_1 than do the experimental curves. Even with allowance for the sparse set of PIC calculations used in the construction of the resonance curves, the theoretical results do not appear to reproduce the experimental observations of pronounced resonances at other than low-density resonance locations. In addition, from Fig. 15, the PIC calculations have a shift in resonance location from that of low-density theory that is more than can be accounted for by variation with V_2, and is similar to that in Fig. 13 for $\nu_1 = 0.4$ MHz.

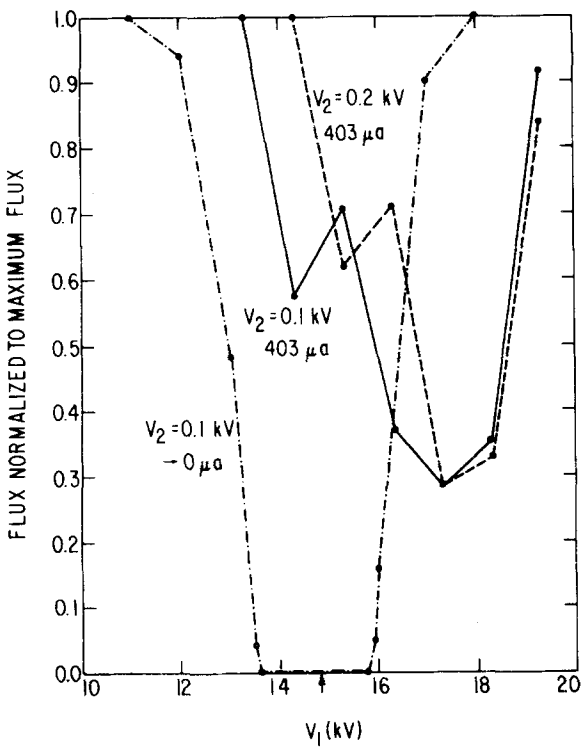

FIG. 15. High-V_1 portion of the resonance curves, normalized to unity for $V_2 = 0.1$ kV (solid curve) and 0.2 kV (dashed curve) as calculated with space-charge coupling, and for $V_2 = 0.1$ kV (dot-dashed curve) as calculated without space-charge coupling. $\nu_1 = 0.8$ MHz, $\nu_2 = 0.0363$ MHz, and I is 403 μA.

2. Analysis

Additional mechanisms of plasma loss induced by the dipole field are responsible for the features of the calculated resonance curves in Figs. 14 and 15, but they are difficult to isolate in the PIC calculations. The problem can be simplified to some degree by calculating plasma behavior in a pure dipole field, i.e., zero quadrupole field or $V_1 = 0.0$ V. In Fig. 16, the results of such a PIC calculation for $V_2 = 0.1$ kV and $\nu_2 = 0.0363$ MHz are presented in terms of the Cs^+ charge distribution for the first four times the applied dipole field passes through zero, i.e., $\frac{1}{4}(1/\nu_2)$, $\frac{3}{4}(1/\nu_2)$, $\frac{5}{4}(1/\nu_2)$, and $\frac{7}{4}(1/\nu_2)$. The arrow indicates the direction in which the applied field has been pushing positive particles since the previous sign change. Also indicated are the UF_6^- and Cs^+ charge distributions in the low-density limit. At each time, only one-half of the charge distribution is displayed; the remaining half can be generated by reflection. The dipole field points along the vertical axis. The lengths between tick marks along the border denote 2.0 cm.

Figure 16 illustrates three important characteristics about ion behavior in a pure dipole field. First, the applied field is strong enough to introduce substantial charge separation in the low-density limit. The overlap of the Cs^+ and UF_6^- distributions in that limit is considerably less than perfect in the figure, and approaches zero at intermediate times not represented in the figure. For $V_1 \leqslant 20$ kV, this charge separation in the low-density limit will not change with the presence of a quadrupole field except near the Cs^+ or UF_6^- resonance, where it will be enhanced by resonance effects. Even though the dipole field strength in Fig. 16 is quite small relative to the quadrupole field strength for most of the resonance curve, the charge separation induced by the dipole field is more substantial than that induced by the quadrupole field. This is a reflection of the fact that the size of V_2 is exceptionally large for the low-density limit. While that size is required to produce a deep resonance at high plasma densities, it is four times larger than the optimal value at low density [Fig. 12(a)].

The second observation concerning Fig. 16 is that at high density, Cs^+ is lost by a process somewhat similar to that seen in the confinement studies (Sec. III D). Since $\nu_p \gg \nu_2$, such a loss is to be expected and presumably should be more complete than in the case of the quadrupole field alone. (The calculations were not carried out over a sufficient simulation time to verify this.) The length of time before substantial plasma loss occurs is an order of magnitude longer in a perfect dipole field for $V_2 = 0.1$ kV than a perfect quadrupole field for $V_1 = 14.8$ kV (compare Fig. 16 with Fig. 6 and recall ν_2 is 11 times smaller than ν_1). The reduced value of V_2 is the apparent cause and a similar increased time for plasma loss is found for reduced values of V_1 in a quadrupole field alone.

The third observation is that the high-density Cs^+ distribution, as a whole, never moves off center of the QMF axis. It follows neither the low-density Cs^+ or UF_6^- distributions, but elongates in both directions along the axis to which the oscillating dipole field is being applied. The reason for this is that the space-charge potential is shielding the bulk

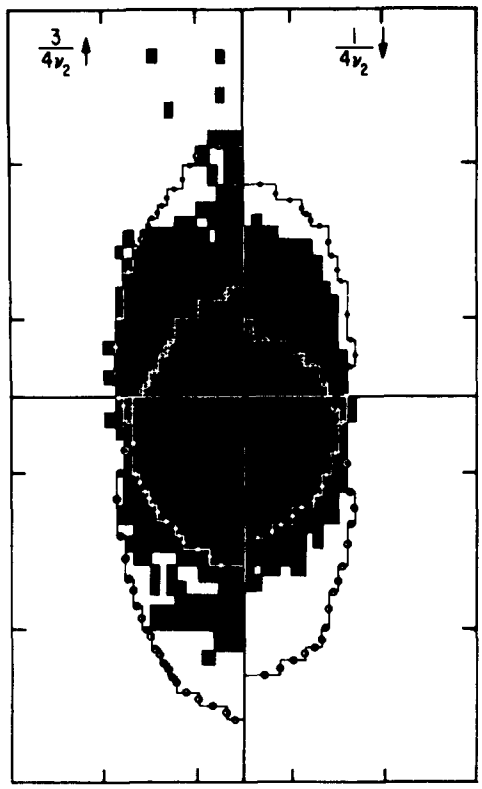

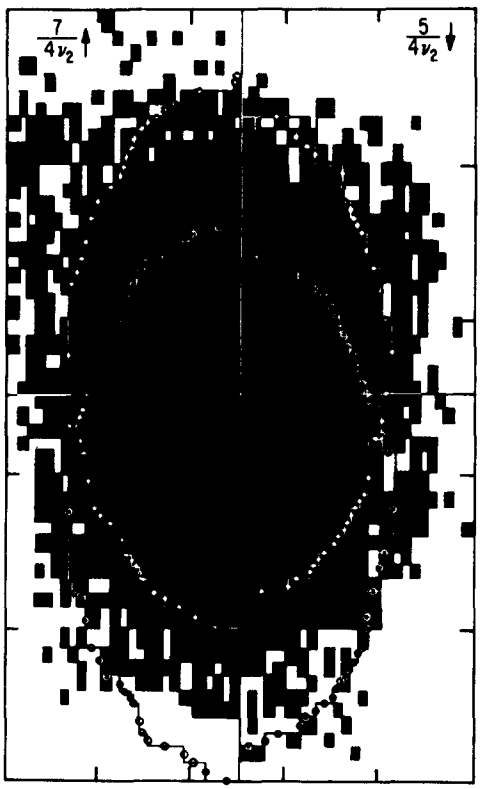

FIG. 16. Calculated symmetric half of the Cs^+ distribution for times $\frac{1}{4}(1/\nu_2)$ and $\frac{3}{4}(1/\nu_2)$ in (a) and $\frac{5}{4}(1/\nu_2)$ and $\frac{7}{4}(1/\nu_2)$ in (b). The dipole field is applied in the vertical direction, $V_2 = 0.1$ kV, and there is no quadrupole field. I is 403 μA. The shaded distribution is that calculated with the PIC model. The outlines of both the Cs^+ (curve with O) and UF_6^- (curve with ●) distribution calculated in the absence of space-charge coupling are plotted. The arrows indicate the most recent direction in which the applied field attempts to push positive charges. Each tick mark in the horizontal and vertical directions denotes 2.0 cm.

of the plasma from the applied field. In Fig. 17, the space-charge potential is displayed for the first two times after the initial time that the applied field is at its maximum, i.e., $1/(2\nu_2)$ and $1/\nu_2$. At each time, only one-half the potential is shown; the other half can be generated by reflection across the vertical axis. The sign of each quadrant of the applied potential at each time is denoted by the plus and minus signs next to the vertical axis. The positive contours of the space-charge potential are beaded curves, while the negative contours are solid curves, and the node between them is sketched in as a dashed curve. The space-charge potential in each quadrant is clearly opposite the applied field and is able to oscillate at the relatively slow frequency of the applied field. Thus the bulk of the plasma is shielded from the full effect of the applied field.

Although Fig. 16 displayed only the high-density Cs^+ distribution, the behavior of the high-density UF_6^- distribution is similar, except that it takes longer for the characteristic features to develop because UF_6^- is heavier and slower than Cs^+. Figures 16 and 17 then suggest that, at high values of V_2, plasma loss is substantial, occurs by loss at the edges with no bulk movement off axis, and involves at least initially greater loss of the lighter ion. With significant plasma loss,

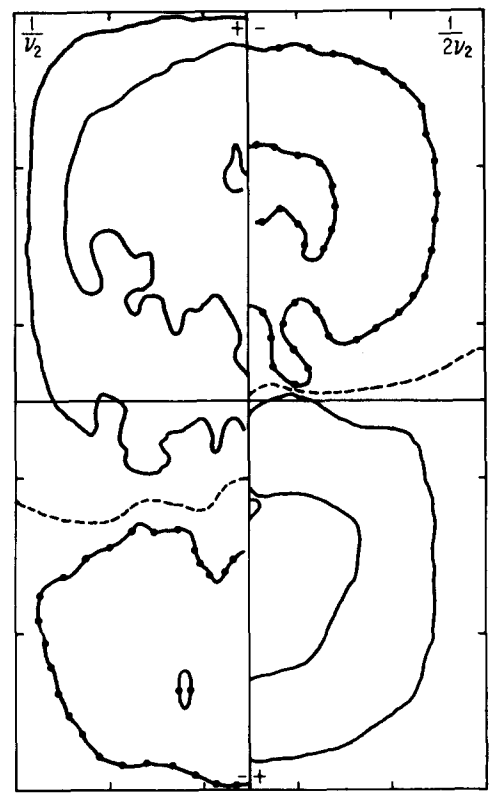

FIG. 17. Symmetric half of the calculated space-charge potential at the times $\frac{1}{2}(1/\nu_2)$ and $(1/\nu_2)$ for the same conditions as Fig. 16. The outermost, middle, and (if present) innermost contours denote equipotentials whose absolute values are 10, 50, and 90% of the calculated maximum absolute value of the potential, respectively. Positive and negative contours are denoted by curves with ● and solid curves, respectively. The dashed curve indicates the zero equipotential line. The + and − near the vertical axis indicates the sign of the applied potential. Each tick mark in the horizontal and vertical directions denotes 2.0 cm.

the plasma density will decrease, eventually permitting penetration of the applied field into the bulk and some movement of the ion distributions as a whole off the QMF axis.

The differences between the confinement and resonance curves in Fig. 14 can now be somewhat better understood. The substantial loss of confinement at low V_1 for high V_2 is a continuation of the loss mechanism in Fig. 16 for $V_1 = 0.0$ V. The dipole field is attempting to induce over most of the range of V_1 very substantial charge separation which results in severe plasma loss until the quadrupole field becomes the dominant applied field and plasma loss becomes more characteristic of the confinement curves. The broad and relatively shallow main UF_6^- resonance at $V_1 \approx 16$ kV requires large values of V_2 because of all the reasons mentioned previously for the case of $\nu_1 = 0.4$ MHz and, in addition, because of the fact that the plasma bulk is initially shielded from the dipole field when its plasma density is high. There is, in fact, some empirical evidence suggesting that V_2 must be, if anything, larger for $\nu_1 = 0.8$ MHz than for $\nu_1 = 0.4$ MHz to achieve a comparably deep resonance (see Figs. 21 and 24 in Paper I). The shift in resonance location for both values of V_2 from the location predicted by low-density theory is similar to what is calculated in the case of $\nu_1 = 0.4$ MHz and like that case, the plasma is generally negatively charged by preferential loss of Cs^+ (for $\nu_1 = 0.4$ MHz, Cs^+ loss is total).

The middle portion of the resonance curve between the Cs^+ and UF_6^- low-density resonance locations is the most difficult to interpret and the least like experiment. While the calculations show a loss of confinement with increased V_2 that is only weakly dependent on V_1, the experiments show the loss occurs by an amalgamation of resonances that is very much dependent on V_1 (see Figs. 20 and 21 in Paper I). A characteristic of the calculated loss of confinement in this region is that the final plasma is positively charged. This is shown in Fig. 18 where the final net charge of the plasma (relative to the initial charge of the Cs^+ distribution) is plotted as a function of V_1. For $V_2 = 0.0$ kV, the figure shows that the final plasma is always negatively charged at all values of V_1, as discussed in Sec. III D. As V_2 increases, only at low and high values of V_1 does the plasma become negatively charged. In the middle region of V_1, the plasma becomes

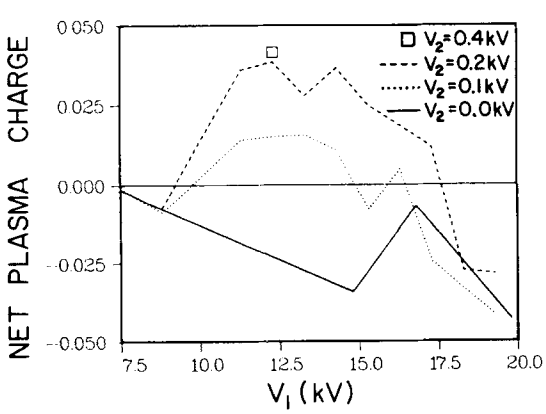

FIG. 18. The final net charge on the plasma (relative to the initial charge of Cs^+) as a function of V_1, for the calculations whose resonance curves are shown in Fig. 14.

increasingly positive with increasing V_2, despite the fact that at the earlier times in all simulations Cs^+ is always lost preferentially. The origin of this effect is not understood at present.

Most likely, the severe numerical compromises necessary to make the PIC calculations feasible resulted in calculated resonance curves that lack both the observed resonance features seen in the middle region of V_1 and the observed sharpness seen in the major resonances at low and high V_1. There were simply too few simulation particles followed over too coarse a space-charge potential grid to reproduce the narrow frequency spectra of the actual plasma. In addition, the shift in resonance position with increased density that was present in the calculations for both $\nu_1 = 0.4$ MHz and $\nu_1 = 0.8$ MHz but not present in the experiments suggests, as mentioned earlier, defects in the calculations beyond numerical accuracy, e.g., oversimplified boundary conditions. Nevertheless, most major features of the resonance curves are qualitatively reproduced by the high-density calculations.

These calculations indicate that resonance behavior for high-density plasmas is qualitatively different from that for low-density ion distributions. The dipole field cannot induce movement of the plasma as a whole at one frequency. Instead, the dipole field contributes to plasma loss mechanisms that reduce plasma density to allow complete penetration by the field. This complex plasma behavior produces a broad spectrum of frequencies for both UF_6^- and Cs^+, which in turn results in broad and shallow resonances.

VII. SUMMARY

The behavior of a Cs^+-UF_6^- ion-pair plasma in a perfect quadrupole field, a perfect quadrupole-dipole field, and in associated fringe fields has been studied at both high and low plasma densities. Trajectory studies in the absence of space-charge potentials confirm all the important experimental observations at low densities in the preceding paper. These include perfect plasma confinement for $\nu_1 = 0.8$ MHz, loss of Cs^+ confinement for $\nu_1 = 0.4$ MHz if $V_1 \gtrsim 10$ kV, sharp resonances for modest values of V_2 when $\nu_f = \nu_2$, and little reflection in fringe fields. Most of the experimental observations at high densities can be accounted for by PIC trajectory studies which include self-consistent space-charge forces. In this context, an idealized two-dimensional PIC model was adopted with simple boundary conditions. The experimental observations reproduced by the PIC model include a plasma confinement that is relatively independent of V_1 for $\nu_1 = 0.8$ MHz; a qualitative drop in UF_6^- confinement and the loss of Cs^+ confinement for $\nu_1 = 0.4$ MHz if $V_1 \geqslant 10$ kV; broad resonances which require large values of V_2; off-resonance loss of confinement at large values of V_2 (especially at small values of V_1); and increasing reflection in fringe fields as V_1 increases. The PIC trajectory studies also produce results that disagree with experiment. These results include the increase in UF_6^- confinement for throughput currents of tens of microamperes with increased V_1 for $\nu_1 = 0.4$ MHz, perfect confinement of UF_6^- at currents of ten microamperes or less for $\nu_1 = 0.4$ MHz, a density-depen-

dent shift in resonance location to higher values of V_1 than that mandated by $\nu_f = \nu_2$, and resonance features for $\nu_1 = 0.8$ MHz less distinct than those seen experimentally. The last result is attributed to economic constraints on the numerical accuracy of the simulation. The other results, by comparison to the UCC model (a model for space-charge effects on a distribution of identical ions), are attributed to various oversimplifications in the idealized two-dimensional PIC model. Finally, the PIC trajectory studies produce a result too difficult to be observed experimentally. This result is the significant loss of plasma at high density for all values of V_1 in a perfect quadrupole field. This loss leads to a predicted limit to transmitted current of several hundreds of microamperes, a limit consistent with but not directly measured by the experiments.

The trajectory studies provide not only results for comparison to experiment but mechanisms for plasma loss in a perfect quadrupole field and resonance degradation in a perfect quadrupole-dipole field. The loss in a perfect quadrupole occurs at densities where the plasma frequency is comparable to the quadrupole frequency. At this density, the applied field can partially penetrate the plasma and loss is not due to thermal blowup. Rather, space-charge effects induce an oscillatory expansion of the edge of the plasma that is periodically reinforced by the applied field resulting in the loss of successive edges of the plasma. This loss continues until the density is reduced to the point that the plasma oscillations are too sluggish to modify the effect of the applied field.

The degradation of the resonance occurs from two effects. First, the loss of plasma at high plasma densities produces highly nonuniform charge distributions with a spectrum of frequencies which results in broader resonances requiring higher values of V_2. This occurs whether or not both Cs^+ and UF_6^- (i.e., a plasma) are present (for $\nu_1 = 0.4$ MHz, only UF_6^- is present). Second, the frequency of the dipole field is considerably below the plasma frequency at the higher densities. Thus penetration by the dipole field is difficult, necessitating large dipole field strengths. At the larger values of V_2, off-resonant plasma loss at the edges occurs as in the case of a quadrupole field alone. Near resonance, the dipole field does not move the resonant ion's distribution as a whole (as occurs at low density) until the density is reduced and penetration becomes more complete. This "evolving" penetration of the bulk plasma also broadens the resonance.

No calculations of $^{235}UF_6^-/^{238}UF_6^-$-$Cs^+$ plasma behavior at high densities were attempted. Experiments discussed in the preceding paper indicate that isotope enrichment based on the low-density theory does not occur at high densities. The theoretical resonance at low density is based on the dipole field moving the ion distribution as a whole. Such does not occur at high plasma density because of penetration problems. In fact, for $\nu_1 = 0.8$ MHz, over most of the calculated resonance, the lighter but off-resonant Cs^+ ion is slightly preferentially ejected over the heavier but resonant UF_6^- ion (i.e., Fig. 18). This suggests that mass-sensitive plasma loss effects dominate mass-sensitive applied-field effects at high densities. If the same reasoning is applied to $^{235}UF_6^-$ and $^{238}UF_6^-$ in a UF_6^--Cs^+ plasma, then, at high plasma density, $^{235}UF_6^-$ would be preferentially lost over the whole UF_6^- resonance. This is, in fact, the experimental observation.

APPENDIX A

A PIC simulation of plasma behavior requires[11] the specification of three parameters which control the numerical accuracy of the simulation. These parameters are: Δt, the time step over which the trajectories are advanced; N_p, the number of simulation particles; and N_c, the number of cells along one side of the square solution region. The value of Δt should be on the order of 0.05 of the period of ion or field oscillations in the plasma.[15] For a plasma in a pure quadrupole field, the two most important oscillations are those characterized by the plasma frequency ν_p [Eq. (12)] and the quadrupole frequency ν_1. For N_p, the value selected should be such that the variation in charge distribution from cell to cell is statistically significant.[16] This generally means most

TABLE IV. N_c, N_p, Δt, and N_t as a function of quadrupole frequency ν_1, current I, plasma radius R_0, and average internal relative velocity $\langle v \rangle$.

ν_1 (MHz)	I (μA)	R_0 (cm)	$\langle v \rangle$ (10^5 cm/sec)	N_c	N_p	Δt (μsec)	N_t
0.8	40	1.0	0.875	568	101 355	0.0625	9 143
			3.554	140	6 158	0.0625	9 143
		3.0	0.875	189	100 999	0.0625	9 143
			10.663	16	724	0.0625	9 143
	400	1.0	0.875	1786	1 002 104	0.0347	16 457
			3.554	442	61 375	0.0347	16 457
		3.0	0.875	599	1 014 486	0.0625	9 143
			10.663	49	6 789	0.0625	9 143
0.4	40	1.0	0.875	568	101 355	0.1087	5 257
			1.777	280	24 632	0.1087	5 257
		3.0	0.875	189	100 988	0.1250	4 572
			5.331	32	2 896	0.1250	4 572
	400	1.0	0.875	1786	1 002 104	0.0347	16 457
			1.777	884	245 500	0.0347	16 457
		3.0	0.875	599	1 014 486	0.1042	5 486
			5.331	98	27 156	0.1042	5 486

occupied cells have about 10 simulation particles. Thus N_p is largely controlled by N_c. N_c is determined[16] by requiring that the spurious oscillatory fields introduced by the discretization of the charge have a wavelength less than the Debye length λ_D. These spurious fields are caused[16] by the fact that two isolated point charges which move so as to preserve their relative separation experience no change in the actual Coulombic force between them but do experience fluctuations in the simulation force due to discretization. For a square region $2r_0$ on a side, N_c should be of order $2r_0/\lambda_D$.

In Table IV, the values of Δt, N_c, and N_p are listed as a function of the quadrupole frequency ν_1, the positive or negative current I, the plasma radius R_0, and the average internal relative velocity $\langle v \rangle$. Also listed is the total number of time steps N_t necessary to follow the plasma for the entire transit time through a 100-cm-long QMF assuming an axial velocity of 1.75×10^5 cm/sec. The values of I, R_0, and $\langle v \rangle$ are the same as those in Table I with the exception that $\langle v \rangle$ is halved in going from $\nu_1 = 0.8$ MHz to $\nu_1 = 0.4$ MHz. Consequently, the values of ν_p and λ_D in Table I (with λ_D halved for $\nu_1 = 0.4$ MHz) are used to determine Δt and N_c in Table IV. Two important points are revealed by the table. First, the size of the calculation is very sensitive to R_0 and $\langle v \rangle$. These quantities are not well known experimentally, and may very well change significantly during the simulation. Therefore, the table values are a guide, but trial runs are necessary in order to determine the degree of accuracy of the computation. Second, the large calculations involving hundreds of thousands of particles, tens of thousands of cells, and ten-thousand time steps are not feasible. Compromises are necessary which reduce the calculations to qualitative rather than quantitative accuracy.

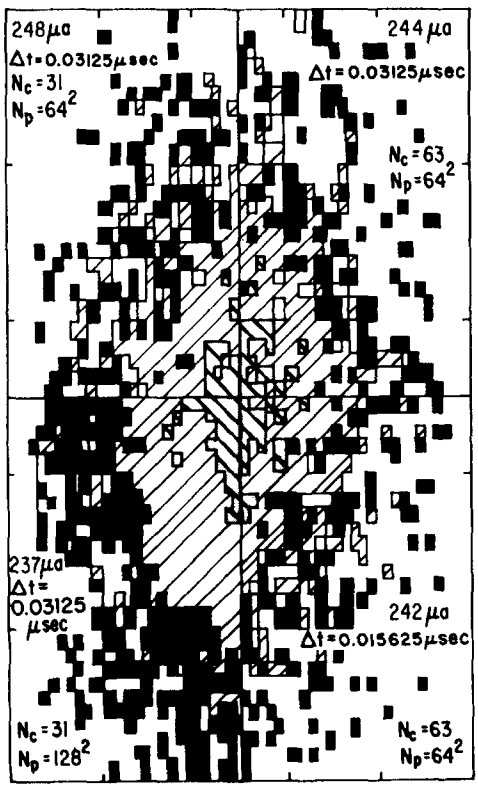

FIG. 19. One quadrant of the UF_6^- charge distribution calculated with the PIC model for a simulation time of 30 μsec for the labelled values of Δt, N_c, and N_p. $I = 403\,\mu$A, $R_0 = 2.0$ cm, $v_\perp = 0.316 \times 10^5$ cm/sec, $\nu_1 = 0.8$ MHz, and $V_1 = 14.8$ kV. The calculated confined flux at 30 μsec is listed in each quadrant. Each tick mark in the horizontal and vertical directions denotes 2.0 cm. Plasma delineations are as in Fig. 8.

In Fig. 19, the calculated UF_6^- distribution after 30 μsec in the QMF is displayed for $\nu_1 = 0.8$ MHz and $V_1 = 14.8$ kV and for calculations in which Δt, N_c, and N_p are varied. I is 403 μA, R_0 is 2 cm, and the initial phase of the applied field is zero. The results in Sec. III D show that many of the basic features of confinement for $\nu_1 = 0.8$ MHz are established by this point in the simulation. Each figure displays a quadrant of the charge distribution for the listed values of Δt, N_c, and N_p. Reflection and inversion symmetry can be used to generate the entire distribution from the displayed quadrant. The charge distributions are derived from computer-generated displays of the number of UF_6^- simulation particles in 0.2×0.2-cm boxes that cover the entire 10×10-cm region indicated by the rectangular border. Note that the x and y scales are not the same, so the border in the figure appears rectangular, but the actual border is square. The tick marks measure off 2-cm increments along each border. The dark heavy lines indicate the x and y axes. The distribution in each quadrant is scaled to the maximum number of simulation particles found in a 0.2×0.2-cm box; the markings indicate occupation by simulation particles numbering within 50% (shaded and lined), 10% (lined), or below 10% (dark) of the maximum.

In the figure, the plasma has suffered losses, and has been reduced to the current listed in the corner of each quadrant. The figure shows that the quoted changes in Δt, N_c, and N_p produce quantitative, but not qualitative, changes in the charge distribution and retained current. In particular, the retained current varies by no more than 3% about the mean of the four calculations, the distributions have all expanded beyond their original radius, and the edges of the distributions are shredded. The lower left-hand quadrant has the most simulation particles and looks the least like the other quadrants. However, most of the difference is in the low-density edge of the distribution; the retained current, which is what is directly comparable with experiment, is little different from the other calculations.

The Cs^+ distributions associated with the UF_6^- distributions in the figure show the same qualitative similarity. Analogous calculations for input currents of 40.3 μA or for $\nu_1 = 0.4$ MHz also show the same qualitative similarity even though the calculated plasma behavior is considerably different. The mechanism for plasma loss at higher densities, as discussed in Sec. III, is also the same for the four calculations used in two figures. Hence all PIC results on confinement used the parameters of the less expensive calculations in the figure, $N_c = 31$ or 63, $N_p = 4096$, and $\Delta t = 0.03125$ μsec (0.0625 μsec for $\nu_1 = 0.4$ MHz). The value of N_c is similar to the values listed in Table IV for a plasma with a relatively large radius and a large amount of relative energy. The charge distributions in the figure indicate this is a reasonable description of the calculated plasma. The value of N_p is on the low side of those listed in the table but as mentioned,

much larger values of N_p do not produce qualitative changes in the results. The value of Δt is somewhat smaller than that listed in the table for reasons that have to do with the calculation of confinement and resonance curves of comparable accuracy (see Appendix B).

APPENDIX B

The same values for Δt, N_p, and N_c tested in Fig. 19 for confinement were evaluated for use in PIC calculations with a combined quadrupole-dipole field. The evaluation consisted of repeating for each set of values a PIC simulation of plasma behavior in the QMF for the case of $\nu_1 = 0.8$ MHz, $V_1 = 17.3$ kV, $\nu_2 = 0.0363$ MHz, $V_2 = 0.1$ kV, $R_0 = 2$ cm, $I = 403\ \mu$A, and zero initial phase of all applied fields. The simulation followed the plasma for 87.5% of the transit time. A quadrant of the final computed UF_6^- distribution for each set of values is displayed in Fig. 20. The retained current of UF_6^- is also displayed in each quadrant. The horizontal and vertical axes are scaled as in Fig. 19. The dipole field has been applied along the vertical axis of the figure. Each quadrant can be reflected about that axis, but not about the horizontal axis because of a reduction in symmetry due to the dipole field. Thus only the same quadrant of the computed distribution is represented for each set of values in the figure. Local density variations are not distinguished as in Fig. 19.

The results of the calculation with the larger number of simulation particles appear to be different from the others in Fig. 20. However, with initially four times as many simulation particles as in the other calculations, in the absence of distinguishing local density variations, a more "filled-in" distribution is to be expected. A more substantial difference is that the distribution for the larger N_p appears more clustered about the vertical axis than the other distributions. However, these differences do not appear to affect the total confined flux which is used to obtain the resonance curves. This flux is very similar for all four calculations.

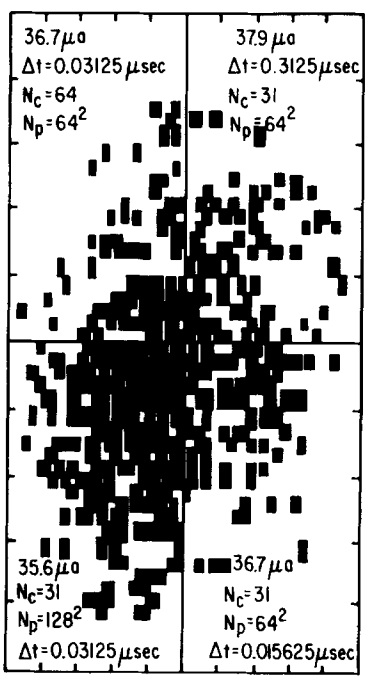

FIG. 20. One quadrant of the UF_6^- charge distribution calculated with the PIC model for a simulation time that is 87.5% of the transit time and for the labelled values of Δt, N_c, and N_p. $I = 403\ \mu$A, $R_0 = 2.0$ cm, $v_\perp = 0.316 \times 10^5$ cm/sec, $\nu_1 = 0.8$ MHz, and $V_1 = 14.8$ kV. The confined flux at 87.5% of the transit time is listed for each calculation. Each tick mark in the horizontal and vertical direction denotes 2.0 cm.

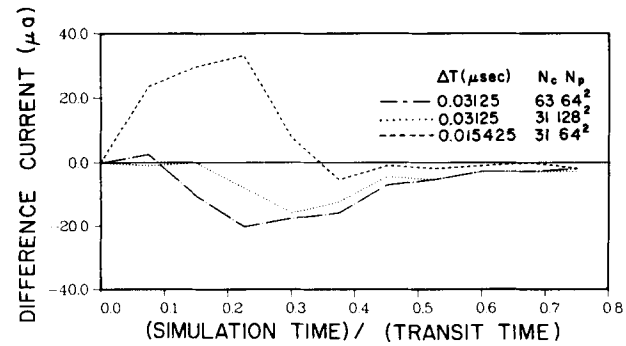

FIG. 21. Differences in confined flux among the several calculations of Fig. 20 as a function of the simulation time relative to the transit time. The standard calculation, represented by the zero base line, is characterized by $(\Delta t, N_c, N_p) = (0.03125\ \mu\text{sec}, 31, 64^2)$. The plotted curves trace the subtraction of confined flux determined by the standard from that determined by the other calculations in Fig. 20.

The results in Fig. 20 suggest that the same values of Δt, N_c, and N_p used in the confinement calculations (see Fig. 19) will produce comparably accurate resonance curves. Such a conclusion is probably not warranted, as is indicated in Fig. 21, where the difference in calculated confined fluxes as a function of the simulation time is displayed for the four calculations in Fig. 20. The least expensive calculation $(\Delta t = 0.03125\ \mu\text{sec}, N_c = 31, N_p = 64^2)$ is the standard from which the difference is determined for the other calculations. (Thus the standard corresponds in the figure to a zero ordinate.) At various intermediate times, the four calculations differ from each other by as much as $50\ \mu$A. Thus the calculations are noticeably different from one another, except at the beginning and the end of the simulation time. Flux differences of $50\ \mu$A are $\sim 10\%$ of the initial flux but are $\sim 25\%$ of the final flux, and thus can qualitatively distort the calculated resonance curve.

All the production calculations in Sec. VI used $\Delta t = 0.03125\ \mu$sec, $N_c = 31$, and $N_p = 64^2$. Such calculations are two to four times less expensive than the other calculations listed in Fig. 20. As the previous discussion makes clear, only the grossest calculated features of the resonance curves can be assumed to be reliable. However, the final curves seem in quite reasonable accord with experiment. Without considerably more extensive testing, the more expensive calculations in Fig. 20 cannot be assumed to be more reliable. Calculations less expensive than the final standard used gave physically unrealistic results.

ACKNOWLEDGMENTS

We wish to express our appreciation to E. K. Parks, C. E. Young, and S. Wexler for extensive and continuing dis-

cussions during the entire course of this work. We also thank L. Rudzinski for important contributions to the computer codes used in this work.

[1]S. Wexler, E. K. Parks, C. E. Young, and R. A. Bennett, J. Appl. Phys. **54**, 1730(1983).
[2]P. H. Dawson and N. R. Whetten, *Advances in Electronics and Electron Physics*, Advances in Electronics and Electron Physics, edited by L. Marton (Academic, New York, 1969), pp. 59–185.
[3]B. K. Annis and S. Datz, J. Chem. Phys. **69**, 2553 (1978).
[4]W. Paul, H. P. Reinhard, and U. von Zahn, Z. Phys. **152**, 143 (1958).
[5]R. F. Lever, IBM J. Res. Dev. **10**, 26 (1966).
[6]P. H. Dawson and N. R. Whetten, J. Vac. Sci. Technol. **5**, 1 (1968); Int. J. Mass Spectrom. Ion Phys. **3**, 1 (1969).
[7]P. H. Dawson, Int. J. Mass Spectrom. Ion. Phys. **14**, 317 (1974); **17**, 423 (1975).
[8]M. Baril and A. Septier, Rev. Phys. Appl. **9**, 525 (1974).
[9]W. M. Brubaker, Adv. Mass Spectrom. **4**, 293 (1968).
[10]P. H. Dawson, Int. J. Mass Spectrom. Ion Phys. **6**, 34 (1971); J. Vac. Sci. Technol. **9**, 487 (1974); Int. J. Mass Spectrom. Ion Phys. **25**, 372 (1977).
[11]R. L. Morse and C. W. Nielson, Phys. Fluids **12**, 2418 (1969).
[12]The relative energy incorporates the 0.3-eV threshold energy for the electron-transfer reaction as measured in Ref. 3.
[13]R. W. Hockney, Methods Comput. Phys. **9**, 135 (1970).
[14]B. L. Buzbee, G. H. Golub, and C. W. Nielsen, SIAM J. Numer. Anal. **7**, 627 (1970).
[15]A. J. Hatch and J. L. Shohet, Phys. Fluids **17**, 232 (1974).
[16]A. B. Langdon, J. Comput. Phys. **6**, 246 (1970).